

## Complexes of semiflexible polyelectrolytes and charged spheres as models for salt-modulated nucleosomal structures

K.-K. Kunze<sup>1</sup> and R. R. Netz<sup>1,2</sup><sup>1</sup>Max Planck Institute of Colloids and Interfaces, 14424 Potsdam, Germany<sup>2</sup>Sektion Physik, Ludwig-Maximilians-Universität, Theresienstrasse 37, 80333 München, Germany

(Received 29 January 2002; published 29 July 2002)

We investigate the complexation behavior between a semiflexible charged polymer and an oppositely charged sphere with parameters appropriate for the DNA-histone system. We determine the ground state of a simple free energy expression (which includes electrostatic interactions on a linear level) numerically and use symmetry arguments to divide the obtained DNA configuration into broad classes, thereby obtaining global phase diagrams. We pay specific attention to the effects of salt concentration, DNA length variation, DNA charge renormalization, and externally applied force on the obtained complex structures.

DOI: 10.1103/PhysRevE.66.011918

PACS number(s): 87.15.-v, 82.70.Dd, 61.25.Hq

### I. INTRODUCTION

Complexes formed between charged polymers and oppositely charged spheres are a common pattern in chemistry, physics, and biology. Electrostatic attraction between the sphere and the polyelectrolyte (PE) leads to more or less tightly wrapped polymer conformations. The most important question is how the polymer conformation depends on the various system parameters such as charge of the sphere and polyelectrolyte, polymer length and sphere diameter, and salt concentration of the surrounding medium.

Typical examples include the wrapping of synthetic PEs around charged micelles [1,2], charged plastic beads [3], or dendrimers [4]. One interesting application of such structures is the fabrication of hollow polymeric shells, which are formed on the basis of multilayer adsorption of charged polymers on oppositely charged colloidal particles [5,6]. Of particular importance in these applications is the phenomenon of overcharging, i.e., in each polymer adsorption cycle more PE adsorbs than is necessary to neutralize the substrate charge, making the formation of charge-oscillating multilayer adsorption possible. In recent investigations, it was found that very small gold particles (with particle diameters down to 10 nm) can be successfully coated only at finite, nonzero salt concentrations [7,8]. On the other hand, it was found that the complexation of PE with charged micelles only occurs below a certain salt concentration [1]. Taken together, these results indicate that PE-sphere complexation is observed for intermediate salt concentration only, an observation that triggered part of the current investigations reported in this paper.

In many experiments and applications, one is considering complexation phenomena in solution, where a dynamical equilibrium between complexed and uncomplexed constituents is present. Owing to the typical broad polydispersity of synthetic polymers, there will be some spectrum of different configurations consisting of one or more spheres bound to a single polymer. On the other hand, especially for synthetic charged colloidal spheres in the micrometer range, more than one polymer will be typically adsorbed. In this paper we exclude those more complicated structures and concentrate

on the problem of a single PE adsorbing on a single sphere.

The same problem in a very different context is encountered with biological complexes formed between DNA, a rather stiff, strongly negatively charged biopolymer, and histone proteins, which are basic globular proteins with a diameter of roughly 10 nm. In the biological context, DNA-histone complexation serves to package DNA in a very efficient way, making it possible to store the roughly 1 m of human DNA in a cell nucleus of a few micrometers in diameter [9–15]. It is now known that the DNA wraps roughly twice around each histone protein, forming the so-called nucleosomes. In the chromatin structure these nucleosomes are arrayed like beads on a string and form various types of higher-order structures depending on the outer conditions. By certain procedures, to be discussed below, the DNA can be cut between the nucleosomes, while leaving the histone proteins and the structure of the adsorbed DNA strand intact. Massive amounts of information is available on the behavior of these nucleosomal particles, which have been studied primarily to understand the behavior of the DNA organization on the lowest hierarchical level. The advantage of such systems for the theoretical modeling is that the DNA can be prepared in an almost monodisperse manner, making comparison with theoretical results meaningful.

Hybrid systems consisting of DNA adsorbed to small positively charged latex particles [16] or dendrimers [17] have also been studied and hold promising potential for gene-technological applications.

On the theoretical side, the adsorption of PEs on charged spheres was studied in a number of previous publications for rather flexible polymers using variational and self-consistent methods [3,18–20], where the adsorbed chain forms a rather homogeneous charge distribution and mean-field-like approximations can be used. A different approach employs the fact that if a polymer with a persistence larger than the sphere radius adsorbs, the polymer density distribution is rather inhomogeneous and (if the adsorption energy is large enough) fluctuations around the optimal path of the polymer are weak, making a ground state analysis quite useful [21–24]. Such studies predict a wrapping transition between a state where the polymer is tightly wrapped around the sphere and a state where the adsorption energy is not large

enough to overcome the bending rigidity (which, in general, contains mechanic and electrostatic contributions) of the polymer. Of particular interest is the effective charge of the complex, since it was realized a few years ago that typically more polymer adsorbs on a charged sphere [23,25–28], cylinder [29,30], or plane [31] than is necessary to neutralize the charged object. Such calculations can be performed without salt ions or counterions [25,26,30], in which case the overcharging is of energetic nature, or in the presence of counterions. In the latter case overcharging can be very large and is obtained already on the linear (Debye-Hückel) level [23,31,30] in the presence of salt, though nonlinear effects associated with counterion release dominate the behavior for highly charged objects at low salt concentrations [29,28]. Monte Carlo studies of the complexation behavior of polyelectrolytes and charged micelles have been performed for various chain models and for different subsets of parameter values [32–36].

For chromatin, i.e., the structure formed by adsorbing many positively charged histone proteins on a single DNA molecule, a number of different theoretical models have been proposed. One class of models tries to understand the structure of chromatin by treating the geometry of a single nucleosome as a parametric input, characterized by a few parameters such as entry and exit angles [37–41]. Other models concentrate on the electrostatic interactions between the charged spheres (or histones) and equilibrate the structure of a single sphere/PE complex [42,43].

In this paper we report calculations of the ground state of a single semiflexible polyelectrolyte of finite length which is in contact with an oppositely charged sphere in the presence of salt. Polymer form fluctuations away from the ground state are neglected, which is an acceptable approximation for rather stiff or highly charged polymers. We specifically consider parameters appropriate for the DNA-histone system, approximating the histone as a uniformly charged, impenetrable, and solid sphere and the DNA as a uniformly charged semiflexible polymer. A brief report of some of our results had been published previously [44]. As one of our main results, we demonstrate that it is possible to classify the complexation behavior by two symmetries, namely, a two-fold rotational symmetry and a mirror symmetry, which can be broken independently. Based on the order parameters connected with these symmetries, we obtain the global phase diagrams as a function of the sphere charge and the salt concentration. We also consider the case of no salt, in which case (since a finite-sized object does not bind its counterions) charges interact via pure Coulomb potentials. We treat the screening due to added salt on the linear (Debye-Hückel) level. Nonlinear effects associated with counterion binding/release are treated using a simple charge-renormalization scheme in Sec. V. Most of our results are obtained for a DNA polymer consisting of 146 base pairs (BP), which corresponds to the length of DNA in the so-called nucleosomal core particles, in Sec. VI we investigate systematically length effects on the wrapping phenomena. In Sec. VII we consider the effects of an externally applied stretching force on the DNA-histone complex structure. Details of the numerical discretization methods are found in the appendixes.

Before we describe our model and results, we give a brief introduction into the biological background and the importance of DNA-histone structures, the extended list of references might serve as a good starting point for further reading and investigation. A physicist not interested in the biological context can skip this section.

#### DNA-histone complexation: Biological background

The length of DNA in eukaryotic cells ranges from 5 mm in yeast to over 1 m in humans to several meters in some plants [45]. The nucleus of the cell, which contains all of the cell's DNA, has a diameter of a few micrometers, calling for some very efficient method of compacting the DNA. This packing strategy in fact consists of several hierarchical levels and involves the negatively charged DNA and basic proteins called *histones*, the resultant multicomponent structure is called *chromatin*. On the highest organization level of chromatin one finds the chromosomal structure, which is realized only during cell division. On the lowest level, DNA is wrapped roughly twice around a histone core consisting of eight proteins, a structural unit called *nucleosome*. The length of DNA in the nucleosomal unit varies in length between 165 BP (yeast) and 240 BP (sea urchin sperm). The length of DNA in a single nucleosome is only a small fraction of the total length of a typical chromosomal DNA molecule, so this pattern is repeated many times along the entire length of the DNA. This structural model is corroborated by direct physical evidence, such as x-ray diffraction [46,47], electron micrography [48,49], and scanning force microscopy [50–52]. On the next-higher level of organization, these nucleosomal particles can at intermediate salt concentrations spontaneously fold into a condensed fiber of 30 nm diameter.

The proteins that form the histone core are termed *H2A*, *H2B*, *H3*, and *H4*. A pair of each of the four protein types is present in the histone octamer, which resembles a disk of diameter 11 nm and thickness 8 nm. The mass of the core histones ranges from about 11 kd to 21 kd and the number of amino acid residues in each of the eight subunits ranges from 102 to 135. A large fraction of amino acids are basic, leading to a substantial positive charge, as we will discuss in more detail later on. Although the core histones differ in sequence they have in common a subdivision of the tertiary structure in three regions. The first region exhibits a folding pattern, which is common for all four histones. The second region is unique for each histone and the third region is a labile terminus varying in length between 13 and 42 residues in different histones [53]. The first region forms the center of the octamer. The third region has the highest distance from the center and is believed to be responsible for interactions with DNA and influence transcription [13]. Histones *H3* and *H4* form a central tetramer to which binds a dimer (*H2A-H2B*) on each side [47,54].

A striking biochemical property of chromatin is its response to nuclease digestion. Free DNA can be cleaved at any of its phosphodiester bonds, which are the repeat units of the backbone of DNA, by, e.g., deoxyribonuclease I (DNase I) or micrococcal nuclease (MNase) [45]. After initial nu-

lease attack of chromatin, gel electrophoresis patterns reveal clearly defined chromatin fragments which contain multiples of a base unit consisting of 165–240 BP, i.e., multiples of nucleosomes [10,45]. Thus, the chromatin structure was shown to suppress nuclease reactions over connected stretches of about 200 base pairs, and it was concluded on this basis even before direct structural evidence was available that DNA in chromatin is organized into repetitive units within which packing hinders access of nuclease.

In the course of continued nuclease digestion, intermediate structures of greater stability with respect to nuclease activity are generated. More extensive nuclease digestion releases individual nucleosomes (consisting of a single histone octamer with DNA wrapped around), and further digestion produces so-called *chromatosomes*, which contain the histone octamer with  $\approx 165$  BP of DNA wrapped around, plus an additional protein *H1* (or its variant *H5*) attached to it. The picture that emerges is that chromatin consists of chromatosomes, which are relatively nuclease resistant, and a variable amount of so-called linker DNA, which is readily digested by nucleases and connects the chromatosomes [11].

Further digestion of chromatosomes leads to the so-called *nucleosomal core particles*. This is a chromatosome that has lost the histone protein *H1* (or its variant *H5*) and ten base pairs from each end of the DNA [11]. It is a rather stable structure consisting of the histone octamer plus 146 base pairs of DNA wrapped around. *H1* extraction leaves the remaining chromatin structure otherwise intact, which suggests that *H1* sits on the surface of the chromatosome. Whereas chromatosomes can differ via different *H1* protein types or arrangements, the nucleosomal core particle is highly conserved in evolution and equal for all eukaryotic cells [46,47]. It is also easily prepared and well defined in content and structure, it has therefore been the subject of most physical and chemical studies of the chromatin structure. Accordingly, in most of this paper, we will concentrate on nucleosomal core particles.

It is now understood that chromatin serves at least two purposes; the compaction of DNA, but also the regulation of DNA repair, transcription, and replication [11,12]. If a eukaryotic gene becomes transcriptionally active, the structure of the chromatin in the neighborhood undergoes structural changes, e.g., repositioning of nucleosomes or loosening of folds in order to accommodate transcription factors (proteins that initiate the transcription process) and RNA polymerase [14,55]. As a matter of fact, the presence of bound histone octamers on the DNA does not necessarily inhibit transcription. The mechanism by which the polymerase is able to transcribe through nucleosome-covered DNA is not fully understood, but probably involves a transient loosening of the nucleosomal DNA structure and possibly also minor conformational changes within the histone octamer in order to accommodate the transcribing polymerase [56]. Transcription can be inhibited, for example, if the nucleosome “sits” on the promoter site (the mark that signals the beginning of a meaningful sequence of base pairs) of the DNA, thereby inhibiting transcription factors or promoters to access the site. On the other hand, transcription can be potentiated by positioning the nucleosome such that the promoter site comes

close to another regulatory factor site, which for free DNA would be 200 base pairs away [13], thereby propelling transcriptional cooperation. Nucleosomes are thus not just featureless inducers of DNA compaction, they are in fact biochemically active complexes.

The DNA that is wrapped around the histone core preserves its helical structure. However, the helical periodicity is slightly changed. Whereas free DNA has a periodicity of about 10.5 base pairs per turn, DNA that is complexed with the histone core has an average helical periodicity of 10.2 base pairs per turn. This change has been observed through various experimental methods [47,57,58]. For the considerations throughout this work it is only important to note that the overall structure of the DNA is not altered much during complexation.

It is commonly believed that part of the biologically significant properties of chromatin can be understood in terms of the properties of the nucleosomal structures, which form the basis and motivation for a host of different experiments performed, which we briefly describe now.

In the first class of experiments chromatin or subunits thereof are subjected to external mechanical stress to test for stress-strain relations and possible disruption of samples. These experiments reveal the forces that stabilize the DNA-histone complex and give insight into the interaction involved between DNA and the histone core. In these experiments, force vs extension curves are established that reveal structural changes of the nucleosome [59–61]. As one of the important results, it was found that the stretching response is markedly different in low and high salt concentration environment, being rather continuous at low salt concentrations, while exhibiting an abrupt transition at a characteristic plateau force at high salt concentrations [59].

The second class of experiments comprises investigations of the stability of the nucleosomal core particle in solution upon changes in core particle concentration, temperature, salt concentration, or *pH* of the solvent. These experiments can be compared to similar experiments done with synthetic materials of which the nature of the interaction is known. Experiments involving changes of *pH* and temperature of the solvent render interpretation of the obtained data difficult [62–65]. For example, changes in *pH* modify the charge of the different ingredients simultaneously and temperature changes not only modify the interaction between the ingredients but also lead to denaturation of proteins and the helical DNA structure. A huge number of experiments were devoted to investigations of the influence of the salt concentration on the nucleosomal core particle stability. Different methods have been employed, among them sedimentation studies [66–69], flow birefringence [70,71], neutron scattering [72], fluorescence [73–79], electrophoresis [80], x-ray scattering [81], and osmometry [82,83]. Some of these results have been summarized [84] and the following main points are interesting for our present investigations: At low salt concentrations, several transitions have been found. One transition has been found at about 1 mM NaCl concentration, which has been agreed upon in the literature [72–74,78]. However, different experimental techniques led to different conclusions about its origin. Monitoring the DNA and his-

tone core simultaneously showed that this transition involves structural changes in both ingredients of the core particle, which can be inhibited by cross linking (i.e., gluing together) the histone octamer [68], thereby indicating that the transition is connected with an expansion of the core histones and simultaneous DNA unfolding. In contrast, neutron scattering experiments led to the conclusion that only DNA unfolding is involved at this transition, leaving the core particle unchanged [72]. Some authors suggest a second transition over a somewhat wider range at slightly higher salt concentration [68,70]. A third transition, found to be at extremely low salt concentration, 0.2 mM NaCl, is irreversible and involves dissociation of the histone core and DNA [76,78]. At high salt concentrations, the situation is somewhat similar to the low-salt regime. For increasing salt concentration one first encounters a change of the structure of the histone core particle. This transition is located in the range between 0.5M and 0.75M by most authors and involves changes in the DNA conformation [67,77,80]. The integrity of the histone core has been either monitored by fluorescence measurements or has been enforced by cross linking the histones. Above a salt concentration of 0.75M, dissociation of the (H2A-H2B) dimers from the (H3-H4)<sub>2</sub> tetramer, dissociation of the oligomers themselves, and dissociation of oligomers from DNA have been observed [77,79,84]. The main effect, however, is the desorption of the DNA from the histone core, meaning that the nucleosomal structure is only stable for intermediate salt concentrations. The strong dependence of the stability of the nucleosomal core particle on the salt concentration of the solvent suggests an electrostatic origin of the predominant interactions, because electrostatic forces are strongly influenced by the presence of mobile cations and counterions, which are introduced in the system through salt. These observations motivated the present model, which treats electrostatic interactions as the primary driving force behind the complexation between DNA and histone core.

The last class of experiments covers chemical modifications of the histones or DNA sequence. These experiments can give an insight into the specificity of interactions and allow for precise alterations of, e.g., the core histone charges. The most prominent modifications are acetylation and phosphorylation of amino acid residues of the histones, i.e., neutralization of a positive charge or addition of a negative charge, respectively. The significance of these manipulations lies in the fact that these modifications are also found *in vivo* and can influence the cell cycle as well as transcription and modification of the DNA [13,85,86]. In the context of possible charge interactions between DNA and histones, these modifications are interesting, because acetylation has an impact on the charge of the basic residues and may account for gene activation or silencing by simple tightening or loosening of folds around histone cores. The change of charge by acetylation at different stages of the cell cycle in systems *in vivo* [86] provides additional support for the assumption of predominant electrostatic interactions between histones and DNA. It also means that in modeling DNA-histone electrostatics, it is a good idea to keep the histone charge as a parameter that is varied in a broad range, as we will now

demonstrate by some explicit examples. The total number of lysine and arginine amino acids in a particular complete histone octamer is 216 [9], which results from 13 lysine and 12 arginine residues in H2A, 20 lysine and 8 arginine residues in H2B, 12 lysine and 18 arginine residues in H3, and 11 lysine and 14 arginine residues in H4. However there are also negatively charged amino acids (aspartate or glutamate) in the histones, namely 9 in H2A, 10 in H2B, 11 in H3, and 7 in H5. Finally, the number of acetylation sites are one in H2A, four in H2B, four in H3, and 4 in H4, and the number of phosphorylation sites are one in H2A and H2B each, two in H3, and one in H4. This brings the total number of charges down to less than half, i.e., 106 net positive charges. Even this number might be too large, since the pH value of arginine is 12.0 and that of lysine is 10, both bases are rather weak and complete dissociation is unlikely due to repulsion between neighboring positive charges and due to image charge effects. Likewise, it was found that trypsination, which cleaves the highly positively charged histone tails off from the histone proteins, leaves the overall shape of the octamer core and of the nucleosomal structure intact [87].

We should also mention that in many studies the DNA-histone complexes have been reconstituted, which allows to study complexes consisting of DNA much longer than occurring in natural nucleosomal core particles [88]. The length dependence of histone-DNA complex stability is therefore of experimental interest and will also be studied in this paper.

Besides the histone proteins, there are many other sequence-dependent DNA binding proteins whose principal function supposedly is to produce DNA bending [89,90]. The bending of the DNA is in these cases produced by proteins with a positive charge much smaller than the histone proteins and can also be addressed in our general model.

## II. MODEL

Designing a simple model that can explain the salt- and charge-dependent behavior of nucleosomal core particles requires a number of approximations concerning the structure of the DNA, the histone octamer, and their interactions. Our strategy is to formulate the simplest possible model which captures the characteristic features responsible for the salt-dependent nucleosomal core structures. In the following we specify the various approximations and their justification.

We describe the nucleosomal DNA by a semiflexible negatively charged polymer of length  $L$  [91,92]. In the most part of this paper we deal with nucleosomal core particles consisting of DNA with 146 BP of length 0.34 nm each, leading to a total DNA length of  $L = 49.6$  nm; in Sec. VI we vary the DNA strand length over a wide range in order to investigate length effects on the stability of DNA-protein complexes. The stiffness of the DNA contains charge-independent and charge-dependent contributions. The former are due to the energy associated with the deformation of hydrogen bonds that stabilize the double helical geometry of DNA and are incorporated by using a semiflexible polymer model with a mechanical bending stiffness. The latter stem from the fact that the negatively charged monomers of the DNA tend to maximize their mutual distance and thus prefer

an extended configuration. This electrostatic contribution decreases with increasing salt concentration of the solution and vanishes at the hypothetical limit of infinite salt concentration [93,94]. The salt-independent mechanical persistence length of DNA is therefore the infinite salt limit of the total persistence length, which has experimentally been determined as  $l_0=30$  nm [95–97]. A discussion of different methods to determine the persistence length of DNA is found in [92]. We take into account the electrostatic contribution to the persistence length by explicitly including the electrostatic self-energy of DNA conformations; we therefore accurately include the scale dependence of the electrostatic contribution on the persistence length [98], which is particularly important in our case since the scale of bending (the histone diameter) becomes of the order of or even smaller than the screening length. Since the ends of the DNA are free to rotate, twist degrees of freedom of the DNA are neglected. Any twist-bend coupling would modify the effective mechanical persistence length. Since we adapt the persistence length from experiment, these effects are implicitly included.

The histone octamer is approximated as a rigid sphere of radius  $R_{\text{hist}}=4$  nm. This is of course only a very rough approximation of the real structure, which is not a perfect sphere and also possesses a very rough surface with specific binding sites for the DNA. Also, any conformational changes of the histone octamer, which do occur for extremely low or high salt concentration, are neglected. The DNA is modeled as a polymer with a radius of 1 nm. In the actual calculation we fix the minimal distance between the sphere center and the DNA monomer centers to be  $R=5$  nm, which is the sum of histone and DNA radii.

The electrostatic interactions between charges on the DNA with each other and the sphere are described by Debye-Hückel (DH) potentials that neglect non-linear effects [such as counterion condensation or counterion release, for which one would need to use the full nonlinear Poisson-Boltzmann (PB) theory [99–101]]. The main reason for this approximation is that the calculation of the optimal DNA configuration within the PB approach is at present numerically not feasible [102]. For large salt concentrations, the DH approximation becomes valid, as has been shown by calculating the electrostatic contribution to the bending rigidity of a charged cylinder [100,101]. The effect of counterion condensation for low salt concentration will be investigated in Sec. V on an approximate level, where we present results taking the charge renormalization of the DNA into account. The main message will be that the phase diagrams are modified, but the general trends are preserved. The presence of water is introduced through a dielectric constant ( $\epsilon \approx 80$ ) which is homogeneous throughout the system. Image charge effects are neglected. In addition, in our model, the interactions between charges on the DNA are not influenced by the presence of the region of excluded salt introduced by the sphere. As was shown on the Debye-Hückel level, this effect modifies the interactions at most by a factor of 2 [103]. We also neglect the presence of additional nonelectrostatic interactions, such as van der Waals forces and hydrogen bonds, since experiments have shown that electrostatic interactions are the driving force for the salt-induced transition we are interested in [84]. Also, we

assume that no sequence specific binding effects between histone and DNA are present. These effects have been reported for some special synthetically produced DNA sequences, and manifest themselves through nucleosomal positioning on the histone octamer [104]. In contrast, naturally occurring DNA strands do not exhibit significant sequence effects [105].

With all these restrictions and simplifications in mind, let us introduce our model. The free energy for a given DNA configuration of internal length  $L$ , parametrized by the space curve  $\mathbf{r}(s)$  and in units of  $k_B T$ , reads

$$F = \frac{l_0}{2} \int_0^L ds \ddot{\mathbf{r}}^2(s) - \frac{l_B Z \tau}{1 + \kappa R} \int_0^L ds \frac{e^{-\kappa[|\mathbf{r}(s)|-R]}}{|\mathbf{r}(s)|} + l_B \tau^2 \int_0^L ds \int_s^L ds' \frac{e^{-\kappa|\mathbf{r}(s)-\mathbf{r}(s')|}}{|\mathbf{r}(s)-\mathbf{r}(s')|}, \quad (1)$$

where we implicitly assume that the DNA molecule is inextensible, i.e.,  $|\dot{\mathbf{r}}(s)|=1$ . The first term describes the mechanical bending energy, proportional to the bare persistence length  $l_0$ , where the curvature  $\ddot{\mathbf{r}}(s)$  is given by the second derivative of  $\mathbf{r}(s)$  with respect to the internal coordinate  $s$ . The second term describes the electrostatic attraction between the sphere and the DNA [106]. The charge of the sphere in units of the elementary charge  $e$  is denoted by  $Z$  and the linear charge density of the DNA (in units of  $e$ ) is denoted by  $\tau$ . The strength of electrostatic interactions compared to thermal energy is measured by the Bjerrum length  $l_B = e^2/4\pi\epsilon\epsilon_0 k_B T$ , which is the distance at which two elementary charges interact with thermal energy; at room temperature in water,  $l_B \approx 0.7$  nm. A key ingredient of the Debye-Hückel theory is the screening of electrostatic interactions, which is quantified by  $\kappa^{-1}$ , the so-called Debye-Hückel screening length. It measures the distance beyond which the interaction between two charges is exponentially damped. For a monovalent salt one finds  $\kappa^2 = 8\pi l_B c$ , where  $c$  is the salt concentration. At 0.1M concentration in water, i.e., at physiological conditions, one has  $\kappa^{-1} \approx 1$  nm. The third term describes the electrostatic repulsion between charges on the DNA. We therefore have two terms that tend to straighten the DNA, namely, the mechanic bending energy and the electrostatic repulsion between DNA monomers. The former is salt independent, whereas the latter loses importance with increasing salt concentration. These repulsions are balanced by the DNA-sphere electrostatic attraction, which favors bending of the DNA in order to wrap it around the sphere, but also gets weaker for increasing salt concentration. It transpires that salt will determine the DNA structures in a rather complicated way, as will be demonstrated by our numerical results.

The DH potentials used in Eq. (1) neglect nonlinear effects. For highly charged cylinders in salt solutions, such as DNA, Manning introduced an approximation scheme to the full nonlinear problem. This approximation is based upon the concept of the so-called Manning transition, which occurs at a threshold linear charge density of  $\tau^* = 1/\ell_B$  and above which a certain fraction of counterions stays bound to the

charged cylinder even in the limit of infinite dilution. From this result, Manning argues that if  $\tau > 1/l_B$ , a sufficient amount of counterions is condensed in a dense layer around the cylinder, such as to renormalize the effective line charge to the threshold value  $\tau^* = 1/l_B$ . A cylinder with this effective line charge can then be described by the Debye-Hückel theory [99]. It can be shown that the radius around the cylinder, beyond which the effective charge picture holds, can be very large [107]. However, the Manning argument serves well as an upper limit for nonlinear effects. It consists of replacing the bare charge density  $\tau$  of the cylinder by  $\tau^* = 1/l_B$  if  $\tau > 1/l_B$  and treating the remaining problem using the Debye-Hückel theory. We follow this recipe in Sec. V. However, as we will discuss in more detail in that section, the Manning procedure becomes unreliable both at very small salt concentrations and at large salt concentrations [100,101]. We therefore use in the main part of this paper Debye-Hückel potentials with the full DNA line charge  $\tau = 2/0.34$  nm, corresponding to the maximal degree of dissociation of DNA.

In analyzing the model defined by Eq. (1) we take advantage of the short length of the DNA strand (in most calculations of the order of 50 nm) compared to the persistence length, which is at least 30 nm. We therefore neglect fluctuations and undulation forces [23] between DNA and the sphere and apply a ground state analysis to the model. This consists of finding the configuration of DNA that minimizes Eq. (1) with the constraints  $|\dot{\mathbf{r}}(s)| = 1$  (no stretching) and  $|\mathbf{r}(s)| \geq R$  (impenetrability of sphere). In the discussion section we will critically discuss this approximation and elaborate on how fluctuations come into play and will modify our results.

Analytical minimization of Eq. (1) is difficult in three dimensions. Even in two dimensions, no closed-form expression for the minimum configuration can be given. Previously we considered a perturbative solution for infinitely long DNA and studied some features, such as complexation behavior and generic shapes for different salt concentrations [23]. In the present work we minimize the functional equation (1) numerically by discretizing the chain of length  $L$  using  $N$  rigid subunits, where the number of our subunits has no relation with the physical monomers of the DNA chain. Each subunit, the lengths of which are not necessarily identical, is characterized by a vector and minimization is then performed in the configuration space of all subunit angles, where the integrals in the electrostatic part of the free energy are replaced by sums over subunits. The presence of the constraints due to the impenetrability of the sphere render the solution of the problem even numerically highly involved. In our numerical minimization we have used the FORTRAN NAG routine E04UCF [108], which is designed to find constrained minima of functions for up to several hundred variables [109]. The routine checks for local minima and finds the global minimum. In the case of coexisting minima, further checks for global minima must be done explicitly. The resulting optimum variables are then processed for a systematic analysis. We found a discretization with 200 connecting vectors (401 variables) to optimally balance accuracy requirements and computer power limitations.

For accuracy tests of the discretization, the reader is referred to Appendix B.

### III. ORDER PARAMETERS

The optimal DNA configuration for given values of the sphere charge  $Z$  and screening length  $\kappa^{-1}$  can be classified by two space symmetries, namely, the mirror symmetry and a twofold rotational symmetry. Either of these symmetries can be either broken or conserved independently, giving a total of four distinct configurations. To unambiguously detect the configurational symmetry, we define two order parameters, which measure the rotational symmetry around an axis and the mirror symmetry. The rotational symmetry is quantified by

$$\eta = \frac{\mathbf{r}(0)^2 - \mathbf{r}(L)^2}{L^2}. \quad (2)$$

This quantity vanishes if an axis through the origin can be found, around which the DNA has twofold rotational symmetry. In general,  $\eta = 0$  not necessarily implies twofold rotational symmetry but in the set of minimal configurations found for Eq. (1) it does, as we explicitly checked.

The mirror symmetry is broken if the DNA is a nonplanar three-dimensional space curve (excluding special structures which are nonplanar but conserve mirror symmetry). We recall some basic notions of the differential geometry of space curves; for more details, see, e.g., [110]. Consider a space curve  $\mathbf{r}(s)$  with  $|\dot{\mathbf{r}}(s)| = 1$ , where  $|\ddot{\mathbf{r}}(s)|$  is the curvature. For nonvanishing curvature, every point on the curve is accompanied by a tripod of unit vectors, which are

$$\mathbf{T} = \dot{\mathbf{r}}(s), \quad \mathbf{N} = \frac{\ddot{\mathbf{r}}(s)}{|\ddot{\mathbf{r}}(s)|}, \quad \mathbf{B} = \mathbf{T} \times \mathbf{N}. \quad (3)$$

The vector  $\mathbf{T}$  is the unit tangential vector to  $\mathbf{r}(s)$ . The vector  $\mathbf{N}$  points from  $\mathbf{r}(s)$  to the center of the circle which approximates the curve at  $s$  up to second order exactly. The center of this circle is  $\mathbf{r}(s) + |\ddot{\mathbf{r}}(s)|\mathbf{N}$ , and  $\mathbf{B}$  is the unit vector perpendicular to  $\mathbf{T}$  and  $\mathbf{N}$ . It is thus perpendicular to the plane in which the approximative circle lies. The projection of  $\dot{\mathbf{N}}$  on  $\mathbf{B}$  is called torsion,  $\omega(s) = \dot{\mathbf{N}} \cdot \mathbf{B}$ . If  $\omega(s) = 0$  for all  $s$ , the curve is a two-dimensional object and lies in the plane of mirror symmetry. It therefore is mirror symmetric with respect to this plane. If it is three dimensional, the mirror symmetry is (for the typical configuration that we obtained) broken and there is an  $s$  for which  $\omega(s) \neq 0$ . We therefore use the quantity

$$\sigma = \frac{1}{L} \int_0^L ds \omega(s) \quad (4)$$

as an order parameter for the mirror symmetry.

With the aid of these two order parameters we distinguish four different symmetry classes which are defined and visualized in Fig. 1. In state (or phase) I, the complex exhibits twofold rotational symmetry around the axis connecting the

Phase	$\eta$	$\sigma$	feature
I	= 0	$\neq 0$	wrapped
II	$\neq 0$	$\neq 0$	3D asymmetric
III	$\neq 0$	= 0	2D asymmetric
IV	= 0	= 0	expanded

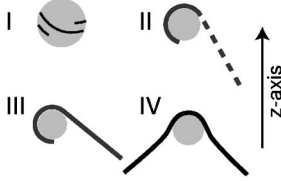


FIG. 1. Characterization of four different symmetry states by the two independent symmetries of twofold rotation (characterized by the order parameter  $\eta$ ) and mirror reflection (characterized by the order parameter  $\sigma$ ).

DNA midpoint and the sphere center. This state always occurs when the DNA is maximally wrapped around the sphere. In state II both symmetries are broken, and in state III only the rotational symmetry is broken while the mirror symmetry is still intact. Phases II and III are intermediate and in the phase diagrams occur between the wrapped state I and the expanded state IV, in which both symmetries are intact. All four symmetry states occur in the phase diagrams and therefore allow straightforward and global classification of the complexation behavior.

#### IV. PHASE BEHAVIOR OF NUCLEOSOMAL CORE PARTICLES

We now turn to our results of the numerical minimization of Eq. (1). In this section, we use the full nominal line charge of DNA,  $\tau=2/0.34$  nm, and therefore neglect counterion condensation effects, which will be discussed in Sec. V. We also confine our analysis for the moment to a DNA strand of length  $L=50$  nm corresponding to 146 base pairs as indeed found in nucleosomal core particles, length dependent effects will be investigated in Sec. VI. We first display real space DNA configurations for vanishing salt concentration at varying sphere charge and after that for varying salt concentration at a few fixed sphere charges. This serves as an illustration of how we deduce the generic phase behavior of DNA-sphere complexes from DNA conformation sequences and order parameter profiles. Thereafter, we present the global behavior of the complex in a globally valid phase diagram.

##### A. No salt

In Fig. 2 we show the DNA configuration, as obtained by minimizing the free energy functional Eq. (1), for a selected set of sphere charges in the case of vanishing salt concentration, i.e.,  $\kappa=0$ , that is, all charges interact via pure Coulomb interactions. It is to be noted that indeed for very small salt concentrations, counterion condensation can be neglected (since a finite length charged cylinder cannot bind its counterions at infinite dilution) and therefore the free energy expression Eq. (1) becomes exact in that limit. For any nonzero sphere charge the DNA bends to some degree around the sphere, i.e., even an infinitesimally small sphere charge breaks the continuous rotation symmetry of the DNA around its long axis. For example, for a sphere charge of  $Z=5$ , the

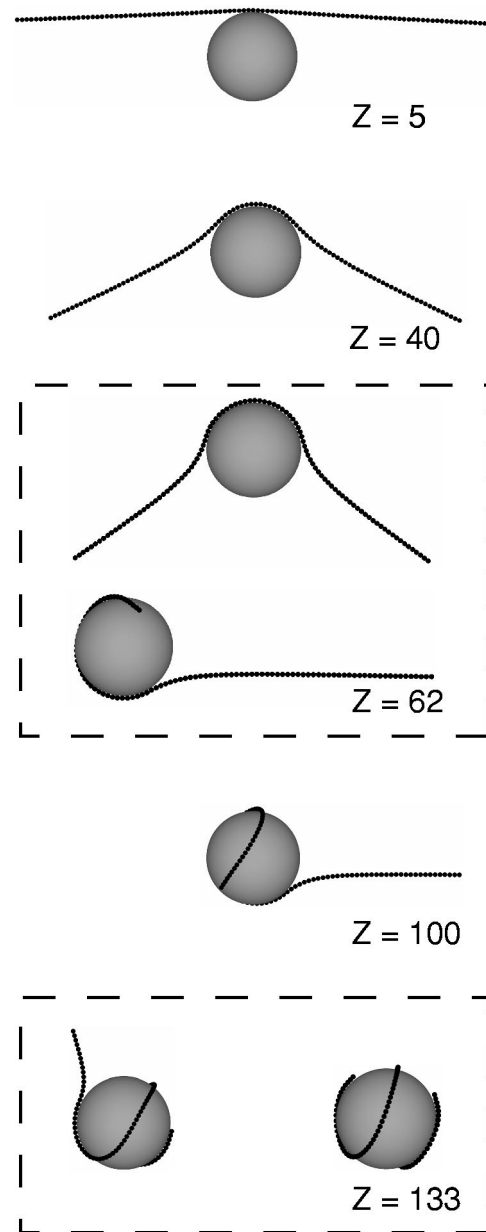


FIG. 2. DNA configurations as obtained by numerical minimization of Eq. (1) for vanishing salt concentration, i.e., pure Coulomb interactions, full DNA charge  $\tau=2/0.34$  nm, and a chain length of  $L=50$  nm. Dashed frames indicate coexisting configurations which have equal energy for one value of the sphere charge  $Z$ .

self-repulsion of the DNA (with a total charge of  $L\tau=292$ ) dominates the energy contributions and the arms show a very weak deflection, see Fig. 2. The configuration still exhibits twofold rotational and mirror symmetry. For  $Z=40$ , both symmetries are still present, but the larger attraction of the sphere leads to an increased deflection of the DNA arms and a larger DNA section which touches the sphere, within which the radius of curvature of the DNA equals the sphere radius. Notice that at larger distances from the sphere, the DNA arms bend away from the sphere. This humplike configuration is characteristic for low salt concentrations and has been initially predicted by analytic perturbation theory (see Fig. 2

of Ref. [23]). At  $Z=62$ , the expanded configuration with rotational and mirror symmetry,  $\eta=0$  and  $\sigma=0$  (phase IV), coexists with a configuration in which both rotational and mirror symmetries are broken,  $\eta\neq 0$  and  $\sigma\neq 0$  (phase II). This value of the sphere charge is therefore the locus of a discontinuous transition between states IV and II. It is remarkable that at salt-free conditions both symmetries are simultaneously broken and, as we will see later on, salt is needed to decouple them. The configuration for  $Z=100$  exemplifies the configuration for intermediate sphere charges: the attraction between DNA and the sphere overcomes gradually the self-repulsion of the DNA, and the extending DNA arm is continuously pulled onto the sphere surface. At  $Z=133$ , rotational symmetry is restored. The three-dimensional (3D) asymmetric configuration (one arm extended, state II) and the state I, in which the DNA is fully wrapped around the sphere, coexist. With a total DNA charge of  $\tau L=292$  this results in an overcharging of the sphere, leading to an effective charge of  $Z-\tau L=-159$  of the complex. For even higher sphere charge than  $Z=133$  the DNA conformation changes very little and remains fully adsorbed on the sphere. Our results are in agreement with the sequence of phases and the overcharging initially predicted by Mateescu *et al.* [25] in the salt-free case for a flexible chain model using analytic and simulation techniques (in that respect, see also the more refined models studied subsequently [26]). Gurovich and Sens [19] studied the adsorption behavior of flexible weakly charged polyelectrolytes on oppositely charged spheres using mean-field theory and find an overcharging of the sphere by a factor of 1.5 of the original sphere charge. We find a factor of  $1.2=(292-133)/133$ , which is surprisingly close given the fact that the chain models used are very different and we are in a situation where mean-field theory is not expected to be valid at all. The good agreement between a host of different models and approximations shows that the overall features of the resulting polymer-sphere complex are rather robust and generic.

In Fig. 3 we show different locally stable configurations at a sphere charge of  $Z=200$  in the absence of screening. The straight-DNA configuration in (a) is included as a reference state, the energy of this state,  $F=-3786$  in units of  $k_B T$ , according to Eq. (1), is obtained by subtracting the self-energy of the straight DNA configuration. Note that the metastable configuration in (c) has twofold rotational symmetry and no mirror symmetry, like the ground state depicted in (d), symmetry class I, and differs by only  $5k_B T$  from the ground state energy. On the other hand, the configuration (b) breaks the rotational symmetry but has mirror symmetry, and shows a three-dimensional structure (this symmetry class was not included in our classification scheme since it was never found to be the ground state). It is of yet higher energy than state (c). It transpires that the simple system consisting of a line adsorbing on a sphere shows a number of different structures and states, and it is clear that one has to take great care not to miss one of the different states which might become the ground state for a restricted range of parameters.

### B. Salt dependence

In Fig. 4 we show configurations for a DNA strand of length  $L=50$  nm and fixed sphere charge  $Z=5$  for inverse

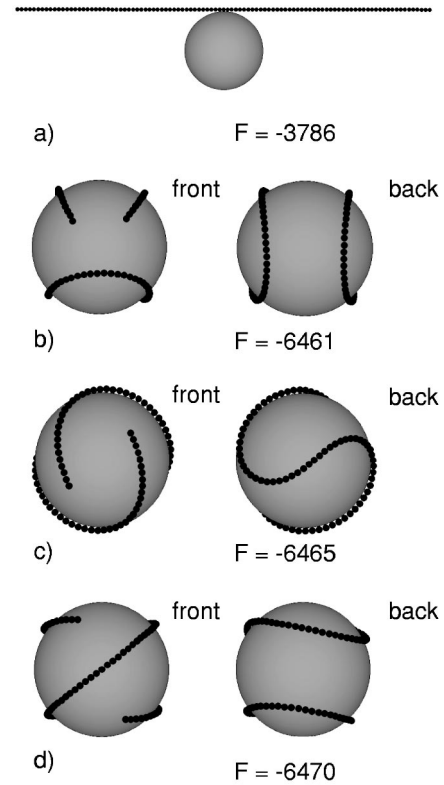


FIG. 3. Different locally stable configurations for a DNA strand of length  $L=50$  nm at a sphere of charge  $Z=200$  and zero salt,  $\kappa=0$ . (a) A straight chain touching the sphere has an energy of  $F=-3786$  in units of  $k_B T$  as compared to a straight chain at infinity. (b) Metastable configuration with an energy which is 0.14% higher than the energy of the ground state in (d). (c) Metastable configuration with an energy which is 0.08% higher than the ground state energy. (d) Ground state.

screening lengths ranging from  $\kappa=0$  nm<sup>-1</sup> to  $\kappa=2$  nm<sup>-1</sup>. This value of sphere charge might be relevant to a class of proteins that bind electrostatically to DNA and perform regulatory functions via induced bending of the DNA [89], as we will comment on at the end of this part. In Fig. 4(a) the Coulomb interaction case (no salt) is shown, which is the same configuration as shown previously in Fig. 2. The arms of the DNA are almost straight, because the strong repulsion between them is only slightly disturbed by the attracting potential of the sphere. In Fig. 4(b) the screening length is equal to the diameter of the sphere. Still, the arms bend only slightly more towards the sphere. At inverse screening length  $\kappa=0.4$  nm<sup>-1</sup>, the repulsion has weakened to an extent that the arms are deflected by an angle of  $\approx 45^\circ$  from the straight configuration. The bending radius of the DNA is everywhere larger than the sphere radius. This behavior, which occurs for small enough sphere charges, was predicted by analytical calculations [23]. For higher salt concentration,  $\kappa=0.82$  nm<sup>-1</sup>, the deflection angle reaches a maximum of  $\approx 90^\circ$ , Fig. 4(d). Note that the screening length is ten times smaller than the sphere diameter, such that the ends of the DNA do not interact with each other. Still, the configuration preserves rotational and mirror symmetry, although the deflection is rather high. Increasing the salt concentration fur-

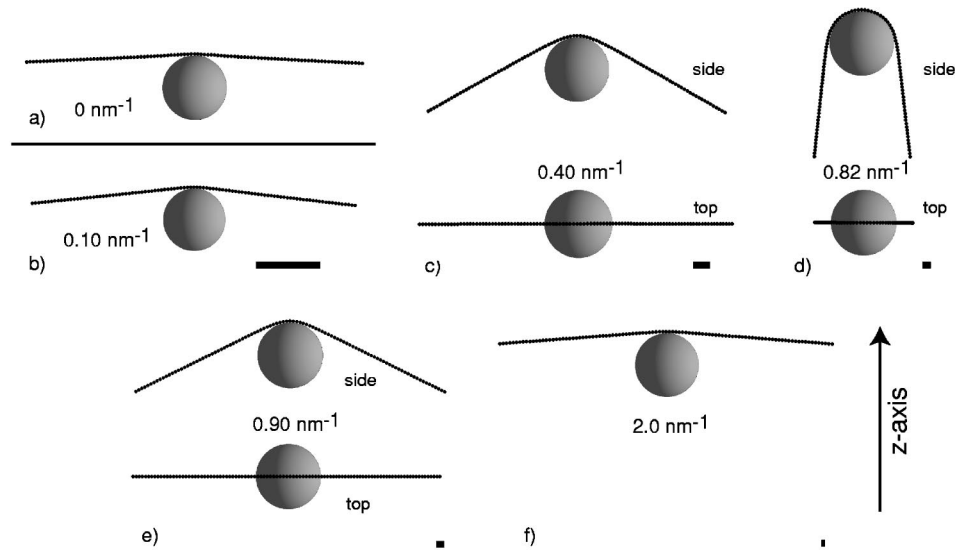


FIG. 4. Configurations for a DNA strand of length  $L=50$  nm as obtained by numerical minimization of Eq. (1) for fixed sphere charge  $Z=5$  and various salt concentrations. Bars on lower right indicate the respective screening lengths (except when infinite). All configurations are rotationally symmetric around the  $z$  axis and mirror symmetric with respect to the paper plane. The  $z$  axis for side views is indicated. (a) No salt. Very weak deflection of DNA arms. (b)  $\kappa=0.1$  nm $^{-1}$  (0.9 mM for monovalent salt), the screening length equals the sphere diameter. (c)  $\kappa=0.4$  nm $^{-1}$  (15 mM for monovalent salt), the arms of the DNA are deflected by approximately  $\approx 45^\circ$  and the DNA touches the sphere only at one point. (d)  $\kappa=0.82$  nm $^{-1}$  (63 mM for monovalent salt), the arms are maximally deflected by  $\approx 90^\circ$  and the DNA consists of a segment which touches the sphere and two almost straight arms. (e)  $\kappa=0.9$  nm $^{-1}$  (76 mM for monovalent salt), the configuration is similar to (c). (f)  $\kappa=2$  nm $^{-1}$  (0.38 M for monovalent salt), the configuration is similar to (a).

ther, as shown in Fig. 4(e) for  $\kappa=0.9$  nm $^{-1}$ , leads to a decrease of deflection. The electrostatic attraction of the sphere is more and more screened and the mechanical persistence starts to dominate the behavior of the system. In Fig. 4(f), we show the configuration for  $\kappa=2$  nm $^{-1}$ . The mechanical persistence of the DNA overwhelms the electrostatic interaction completely. The top views of some of the configurations show that mirror symmetry is never broken. It is interesting to note that configuration (b) is similar to configuration (f) and configuration (c) is similar to configuration (e). For low enough sphere charge, therefore, a certain configuration can be produced by two distinct values of the salt concentration. As a main result, we note that in order to obtain maximal bending of the DNA, the screening length has to be almost ten times smaller than the sphere diameter. Naively, one would expect the optimal balance between electrostatic bending energy and electrostatic attraction energy to be realized when the screening length equals the sphere diameter, and on the scaling level, i.e., neglecting prefactors of order unity, this is indeed borne out by our explicit calculations. Looking more closely, the deviation from the naive expectation can be quite relevant when strong bending of charged polymers around small spherical objects is the goal. Coming back to the biological application alluded to in the beginning of this section, it transpires that a maximal bending of the DNA can be achieved with a charge on a spherical protein as low as five elementary charges *if and only if the salt concentration is adjusted*. For our specific system parameters, the maximal bending indeed occurs at a salt concentration close to physiological conditions, which sheds some light on how rather weakly charged proteins can induce large bends on DNA with the aid of a screening environment [89].

The behavior becomes more complex as the sphere charge is high enough to induce symmetry transitions of the complex. In Fig. 5 we show a series of DNA configurations obtained for a fixed sphere charge  $Z=20$  and for inverse screening lengths ranging from  $\kappa=0$  nm $^{-1}$  to  $0.7$  nm $^{-1}$ . In Fig. 5(a) the pure Coulomb case with no added salt is shown. The deflection of the DNA arms is intermediate between the configurations for  $Z=5$  and  $Z=40$  shown in Fig. 2. As the salt concentration is increased from  $\kappa=0$  to  $\kappa=0.15$  nm $^{-1}$ , the deflection of the DNA arms increases continuously, similar to the case  $Z=5$  discussed in Fig. 4. In between  $\kappa=0.15$  nm $^{-1}$  and  $\kappa=0.16$  nm $^{-1}$  a continuous transition occurs, at which the twofold rotational symmetry is being broken. The two configurations in (b) show that the mechanism of this transition involves the growth of the length of one of the arms at the expense of the length of the other arm, a process that clearly diminishes the electrostatic repulsion between the two deflected arms. Upon increase of salt concentration, going from (b) to (c), the length of the longer arm keeps increasing, while the shorter arm wraps around the sphere. In between  $\kappa=0.30$  nm $^{-1}$  and  $\kappa=0.31$  nm $^{-1}$  the mirror symmetry is continuously broken. The configuration at  $\kappa=0.30$  nm $^{-1}$ , (c), clearly shows that in the planar configuration the shorter arm gets very close to the longer arm, and the breaking of the mirror symmetry, i.e., the escape to the third dimension, can be viewed as a means to minimize the electrostatic repulsion between the short and the long arms, at the expense of increased mechanic bending rigidity. As  $\kappa$  is increased further, the extended arm is more and more pulled onto the sphere, as shown in (d). A slightly discontinuous transition between states II and I takes place at  $\kappa=0.624$  nm $^{-1}$ , the two configurations in (d) at  $\kappa$

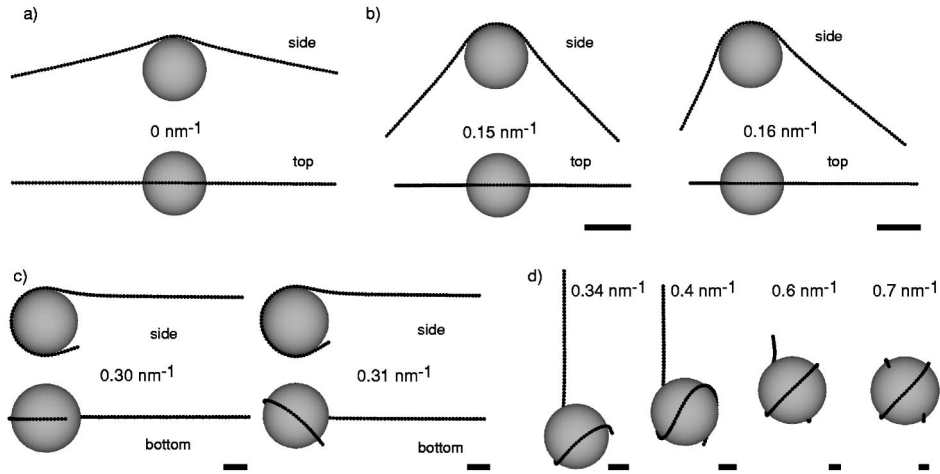


FIG. 5. Configurations for a DNA strand of length  $L = 50$  nm as obtained by numerical minimization of Eq. (1) for fixed sphere charge  $Z = 20$  and various salt concentrations. Bars on lower right indicate the respective screening lengths (except when infinite). (a) No added salt,  $\kappa = 0$ , the configuration shows rotational and mirror symmetry. (b) Configurations at  $\kappa = 0.15 \text{ nm}^{-1}$  (2.1 mM for monovalent salt) and at  $\kappa = 0.16 \text{ nm}^{-1}$  (2.4 mM for monovalent salt), in between of which a continuous breaking of the rotational symmetry occurs. Mirror symmetry is conserved, as the top views show. (c) Configurations at  $\kappa = 0.30 \text{ nm}^{-1}$  (8.5 mM for monovalent salt) and at  $\kappa = 0.31 \text{ nm}^{-1}$  (9.1 mM for monovalent salt), in between the mirror symmetry is continuously broken. (d) Intermediate configurations at  $\kappa = 0.34 \text{ nm}^{-1}$  (10.9 mM for monovalent salt),  $\kappa = 0.4 \text{ nm}^{-1}$  (15.1 mM for monovalent salt), and  $\kappa = 0.6 \text{ nm}^{-1}$  (34.1 mM for monovalent salt). The discontinuous transition from the 3D asymmetric (symmetry class II) to the wrapped configuration (class I) takes place at  $\kappa = 0.624 \text{ nm}^{-1}$  (36.9 mM for monovalent salt).

$= 0.6 \text{ nm}^{-1}$  and  $\kappa = 0.7 \text{ nm}^{-1}$  demonstrate that this transition consists merely of the one short extending arm being adsorbed onto the sphere, thereby restoring the twofold rotational symmetry.

The behavior is qualitatively similar at a higher sphere charge of  $Z = 40$ , for which we show a selection of significant configurations in Fig. 6. In (a) the pure Coulombic case

without screening is shown, identical to the configuration already displayed in Fig. 2. The DNA shows twofold rotational symmetry around the  $z$  axis and mirror symmetry. The pronounced Coulomb repulsion between DNA segments bends the two arms away from the sphere. This behavior is generic for sphere charges that can (for some range of salt concentrations) induce symmetry transitions and screening

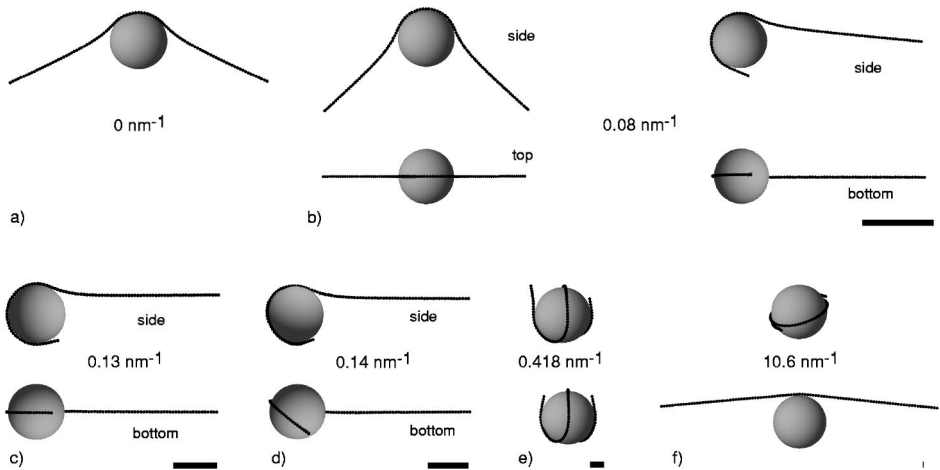


FIG. 6. Configurations for a DNA strand of length  $L = 50$  nm as obtained by numerical minimization of Eq. (1) for fixed sphere charge  $Z = 40$  and various salt concentrations. Bars on lower right indicate the respective screening lengths (except when infinite). (a) No added salt,  $\kappa = 0$ , the resulting configuration shows rotational symmetry and mirror symmetry. (b) At  $\kappa = 0.08 \text{ nm}^{-1}$  (0.6 mM for monovalent salt) the rotational symmetry is discontinuously broken and both the structures shown coexist. The DNA is still mirror symmetric as demonstrated by the top and bottom views. At  $\kappa = 0.13 \text{ nm}^{-1}$  (1.6 mM for monovalent salt) the mirror symmetry is continuously broken. (c) Shows the mirror symmetric configuration right at the transition, (d) shows the mirror asymmetric configuration at a slightly elevated salt concentration  $\kappa = 0.14 \text{ nm}^{-1}$ . (e) At  $\kappa = 0.418 \text{ nm}^{-1}$  (16.6 mM for monovalent salt) the rotational symmetry is restored in a weakly discontinuous transition, as witnessed by the two coexisting structures which are rather similar. (f) Coexistence between fully wrapped and expanded conformation at  $\kappa = 10.6 \text{ nm}^{-1}$  (10.6 M for monovalent salt).

lengths larger or roughly similar to the sphere diameter, i.e., for  $2R < \kappa^{-1}$ . At a slightly elevated salt concentration, Fig. 6(b), the rotational symmetry is discontinuously broken, in contrast to the sphere charge  $Z=20$ , where this transition was found to be continuous. The expanded configuration, to the left, coexists with a configuration where one arm is wrapped around the sphere while the other extends straight away from the sphere, to the right. From the top and bottom views of the complex it can be seen that mirror symmetry is preserved. At  $\kappa=0.13 \text{ nm}^{-1}$  this mirror symmetry is continuously broken, similarly to the case  $Z=20$ . Figure 6(c) shows the mirror symmetric configuration at the transition, Fig. 6(d) shows the mirror asymmetric configuration at a slightly elevated salt concentration  $\kappa=0.14 \text{ nm}^{-1}$ . It is seen that the wrapped DNA arm moves out of the plane of symmetry. In the salt concentration range between  $\kappa=0.13 \text{ nm}^{-1}$  and  $\kappa=0.42 \text{ nm}^{-1}$  the free arm of the DNA is continuously drawn towards the sphere, but no symmetry change takes place. At  $\kappa=0.42 \text{ nm}^{-1}$  the rotational symmetry is restored in a weakly discontinuous transition. The two coexisting structures shown in Fig. 6(e) are rather similar and correspond to a more or less fully wrapped state. In the salt concentration range between  $\kappa=0.42 \text{ nm}^{-1}$  and  $\kappa=10.6 \text{ nm}^{-1}$  the DNA is tightly wrapped around the sphere. At  $\kappa=10.6 \text{ nm}^{-1}$  a strongly discontinuous transition occurs in which the DNA completely dewraps from the sphere. Figure 6(f) shows the two coexisting states. The dewrapped state at high salt concentration is markedly different from the state at low salt concentration shown in Fig. 6(a): There is only one short region of nonzero bending of the DNA connecting two basically straight arms. This sequence of complexation structures demonstrates one of our main results, namely, that the wrapped DNA conformation is only stable for intermediate salt concentrations, explaining a large set of experimental results for nucleosomal core particles [84].

In Fig. 7 we show for  $Z=20$  how the order parameters  $\eta$  (broken line, right axis) and  $\sigma$  (solid line, left axis) reflect the symmetry transitions of the configurations depicted in Fig. 5. For very small salt concentrations, both order parameters vanish, the complex is fully symmetric. At  $\kappa \approx 0.15 \text{ nm}^{-1}$ , the continuous phase transition to the rotationally asymmetric configuration manifests itself through a continuous increase of the order parameter  $\eta$  to a finite value. The continuous breaking of the mirror symmetry at  $\kappa=0.30 \text{ nm}^{-1}$  appears as a continuous but very steep growth of  $\sigma$  (which at this scale appears discontinuous but on a smaller scale can be shown to be continuous). At  $\kappa=0.624 \text{ nm}^{-1}$  the rotational symmetry is restored, which is indicated by the discontinuous vanishing of  $\eta$ . As is expected for systems of several order parameters, transitions in  $\sigma$  have an impact on  $\eta$  and vice versa.

The behavior of the order parameters for  $Z=40$  shown in Fig. 8 is rather similar to the case  $Z=20$  and corresponds to the sequence of real space DNA configurations shown in Fig. 6. The major difference from the results for  $Z=20$  is that at  $\kappa=0.08 \text{ nm}^{-1}$ , the phase transition to the 2D asymmetric configuration is now discontinuous, which manifests itself through a jump of the order parameter  $\eta$  to a finite value. The continuous character of the transition between symmetry

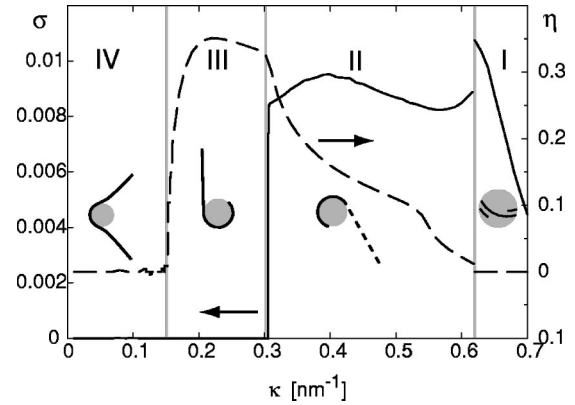


FIG. 7. Rotational order parameter  $\eta$  (dashed line) and torsional order parameter  $\sigma$  (solid line) for fixed sphere charge  $Z=20$  for different salt concentrations. The icons represent all different symmetry states, from left to right: expanded ( $\eta=0$ ,  $\sigma=0$ ; class IV), 2D asymmetric ( $\eta \neq 0$ ,  $\sigma=0$ ; class III), 3D asymmetric ( $\eta \neq 0$ ,  $\sigma \neq 0$ ; class II), wrapped ( $\eta=0$ ,  $\sigma \neq 0$ ; class I). The transition between phases IV and III as well as the transition between phases III and II is continuous, while the transition between phases II and I is weakly discontinuous.

states III and II can now be clearly discerned, while the character of the transition between states II and I is unchanged.

### C. Phase diagram—global aspects

After demonstrating the benefit of the two order parameters, we can use them together with energy considerations to explore the global phase diagram of the system. We summarize our results for a DNA length of  $L=50 \text{ nm}$  in the phase diagram presented in Fig. 9. In Fig. 9(a) we show the transition from the wrapped state ( $\eta=0$ ,  $\sigma \neq 0$ , class I) to the 3D asymmetric state ( $\eta \neq 0$ ,  $\sigma \neq 0$ , class II) without exhibiting transitions between states II, III, and IV, which we denote indiscriminately as *unwrapped* in the phase diagram. In the absence of salt,  $\kappa=0$ , this transition occurs at  $Z=133$ , see Fig. 2. In agreement with experiments [84], complexation is

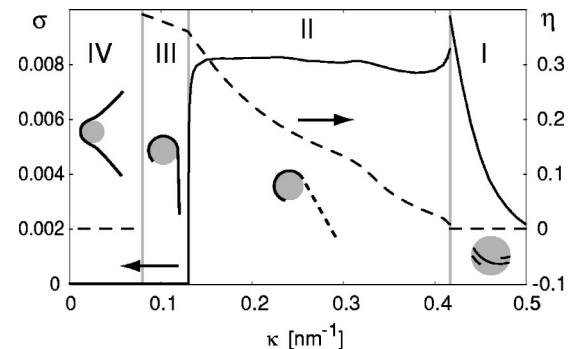


FIG. 8. Rotational order parameter  $\eta$  (dashed line) and torsional order parameter  $\sigma$  (solid line) for fixed sphere charge  $Z=40$  for different salt concentrations. In contrast to the results in Fig. 7, the transition between phases IV and III is now discontinuous while the transition between phases III and II is still continuous. The transition between phases II and I is weakly discontinuous.

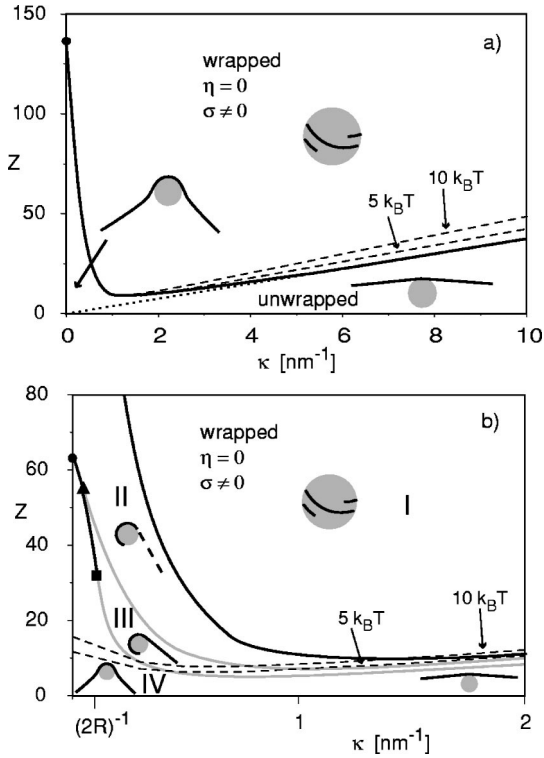


FIG. 9. Phase diagram for a DNA strand of length  $L=50$  nm as a function of sphere charge  $Z$  and inverse screening length  $\kappa$ . (a) The solid line indicates the transition from the wrapped state ( $\eta=0$ ,  $\sigma\neq 0$ , phase I) to the 3D asymmetric state ( $\eta\neq 0$ ,  $\sigma\neq 0$ , phase II). The dotted line is a local-energy-balance argument for this wrapping transition, valid for large salt concentrations. The minimal sphere charge to wrap the DNA is  $Z\approx 10$  and occurs at a screening length  $\kappa^{-1}\approx 1$  nm, roughly corresponding to physiological salt condition. (b) Detail of phase diagram for small  $\kappa$ , featuring all four different phases. Discontinuous (continuous) transitions are denoted by black (gray) solid lines. The dashed lines in (a) and (b) indicate a complexation energy of  $5k_B T$  and  $10k_B T$  (see text).

most pronounced at intermediate salt concentrations. For low salt concentration, the strong DNA-DNA repulsion prevents complexation, for high salt screening it weakens the DNA-sphere attraction sufficiently so that the mechanical bending resistance induces unwrapping. The minimal sphere charge to wrap the DNA,  $Z\approx 10$ , is obtained for  $\kappa^{-1}\approx 1$  nm ( $c\approx 0.1M$  for monovalent salt), corresponding to physiological conditions. Since the total charge on the DNA is about 300, the complex is strongly overcharged for all  $Z<300$ , i.e., in the whole region of the state I shown in the phase diagram. The dotted line is the high-salt prediction for the wrapping transition obtained from locally balancing the various terms in the free energy, Eq. (1), namely, the bending energy per unit length,  $F_{\text{bend}}\approx l_0/2R^2$ , and the electrostatic attraction per unit length in the limit  $\kappa R>1$ ,  $F_{\text{att}}\approx l_B Z\tau/\kappa R^2$ , leading to  $Z_{\text{wrap}}\approx l_0\kappa/2l_B\tau$  [23]. Note that the repulsion between DNA segments, i.e., the electrostatic contribution to the bending energy, can be neglected for large enough salt concentrations. This prediction agrees well with our numerical results for large salt concentration, as can be seen from how the numerical results (solid line) approach the dotted line in Fig.

9(a), and also with experimental results for the complexation of polyelectrolytes with charged micelles [2]. Figure 9(b) shows an enlarged view of the low- $\kappa$  region including all symmetry-breaking transitions. The bottom line denotes the transition from the expanded state ( $\eta=0$ ,  $\sigma=0$ ; phase IV) to the 2D asymmetric state ( $\eta\neq 0$ ,  $\sigma=0$ ; phase III). This transition is continuous below  $Z=34$  (denoted by gray color) and discontinuous (denoted by black color) above, the tricritical point is denoted by a square. The middle line is the transition between the 2D asymmetric state ( $\eta\neq 0$ ,  $\sigma=0$ ; phase III) and the 3D asymmetric state ( $\eta\neq 0$ ,  $\sigma\neq 0$ ; phase II); it is continuous and terminates at a critical end point (denoted by a triangle) at a sphere charge  $Z=55$ . Between  $Z=55$  and  $Z=62.5$  there is a direct, discontinuous transition between the expanded ( $\eta=0$ ,  $\sigma=0$ ; phase IV) and the 3D asymmetric state ( $\eta\neq 0$ ,  $\sigma\neq 0$ ; phase II). The upper line in Fig. 9(b) is the same line drawn in Fig. 9(a). The three phase transitions do not meet, even at high salt concentrations. The true histone charge is not known precisely, as discussed in detail in the Introduction, besides, our calculations neglect counterion condensation on the sphere. The value of the sphere charge in our calculation can thus be viewed as a phenomenological parameter which is only indirectly related to the nominal histone charge. For  $Z\approx 12$ , we predict a fully wrapped complex for a range of salt concentrations between 4 mM and 900 mM, close to experimental values for the DNA-histone release thresholds [84]. The nominal histone charge is certainly higher than 12 unit charges, but it is certainly tempting (though fraught with danger) to use this value as the effective histone charge within our model. We will come back to this value when we analyze the plateau stretching force for histone dissolution, which has recently been determined experimentally. The broken lines in Fig. 9 denote lines of constant complexation energy of  $5k_B T$  and  $10k_B T$ . The complexation energy is defined as the difference of the free energy Eq. (1) in the ground state and the reference state consisting of the straight DNA strand touching the sphere, as, for example, shown in Fig. 3(a). It is seen that the complexation free energy is much larger than  $k_B T$  except very close to the high-salt wrapping transition. This shows that thermally induced unwrapping can be neglected in the main part of the phase diagram, except at very low histone concentrations.

#### D. Phase diagrams—details

In the following, we give numerical details of the analysis that led to the phase diagram shown above. A reader not interested in some of these subtleties can skip this section without loss of overall understanding. We start by examining the transition at which the rotational symmetry is broken (phase IV/phase III). This symmetry transition starts at vanishing salt,  $\kappa=0$ , at a sphere charge of  $Z=62$ , for increasing salt concentration the transition value of the sphere charge decreases steeply until it reaches a minimum at  $Z=5$ ,  $\kappa=0.7$  nm $^{-1}$ , beyond which it increases slightly, see Fig. 9. As is already clear from the behavior of the order parameter plots, Figs. 7 and 8, this transition exhibits a tricritical point at a sphere charge  $Z=34$ , at which the transition changes

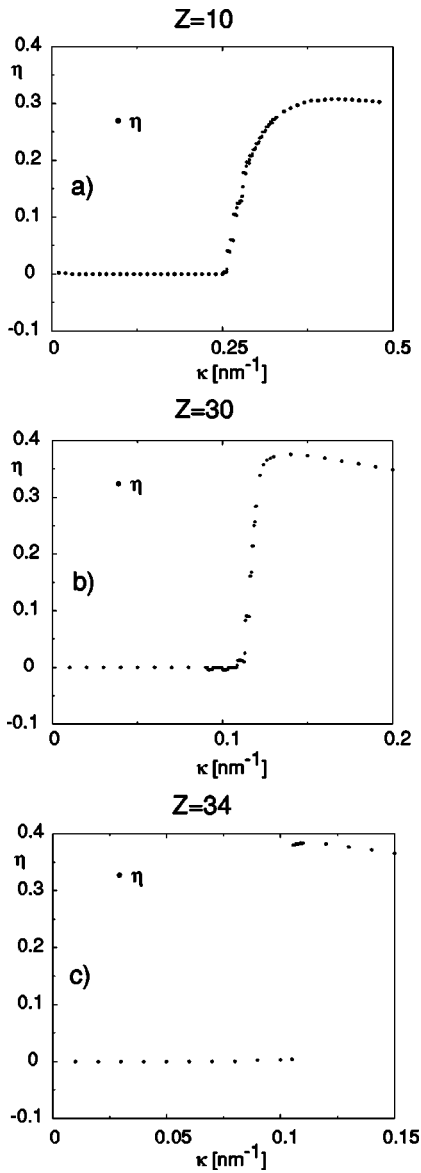


FIG. 10. Breaking of rotational symmetry. Every point denotes the order parameter value  $\eta$  for an equilibrium DNA configuration for a strand of length  $L=50$  nm of Eq. (1) for fixed sphere charge and varying salt concentration. All configurations exhibit mirror symmetry ( $\sigma=0$ ). (a) At  $Z=10$  and  $\kappa=0.261$   $\text{nm}^{-1}$ ,  $\eta$  continuously assumes positive values. (b) At  $Z=30$  and  $\kappa=0.11$   $\text{nm}^{-1}$ ,  $\eta$  assumes positive values continuously but steeper. (c) At  $Z=34$  and  $\kappa=0.105$   $\text{nm}^{-1}$ ,  $\eta$  jumps to the almost maximal value of the order parameter, indicating the presence of a tricritical point at a slightly smaller value of the sphere charge. Discretization effects manifest themselves via formation of small, discrete steps (see text).

from being continuous to being discontinuous. In Figs. 10(a)–10(c), we show the behavior of the order parameter at different fixed sphere charges and varying inverse screening length. At sphere charges below  $Z=34$  the transition is continuous. The variation of  $\eta$  with  $\kappa$  gets more and more steep as  $Z$  increases, as is obvious from Figs. 10(a) and 10(b). Above  $Z=34$  the transition is strongly discontinuous, demonstrated in Fig. 10(c).

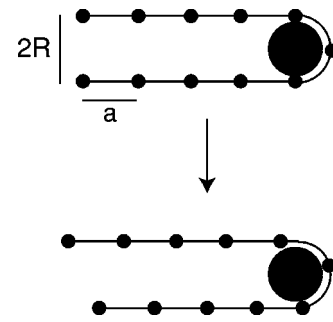


FIG. 11. Discretization effects induce discontinuous configurational changes. Energetically unfavorable DNA configuration (top) vs favorable DNA configuration (bottom) with arms at distance  $2R$  and equidistant charges at spacing  $a$  (DNA charges denoted by small filled circles).

The study of this symmetry transition is made complicated by the fact that discretization effects distort the results we expect to find for a continuous system. We shall therefore comment on the methods used to extrapolate our results for (necessarily) discrete systems to the continuum limit. The key to understanding the discretization effects of the order parameter  $\eta$ , which become more pronounced for higher sphere charge and which lead to the horizontal steps that can be seen in Figs. 10 (a) and 10 (b), lies in the self-interaction of the DNA. Breaking the rotational symmetry can be understood as a sliding of the DNA along the sphere, see, for example, Fig. 5(b). This leads to an interdigitation effect between DNA legs, which results from the discretized charge distribution along the polymer, as is demonstrated in Fig. 11. If two parallel rods with equally spaced charges at distance  $a$  are at distance  $2R$  from each other, but can slide laterally, they will prefer a conformation where the distance between opposite charges is not  $2R$  but  $\sqrt{4R^2+a^2}/2$ . This introduces an energy barrier for every sliding of the DNA arms along each other and introduces a discrete sliding step of width  $a$ . Since the legs of the DNA come closer to each other at increasing sphere charge (cf. Figs. 4 and 6) the effect gets more pronounced as  $Z$  increases. Introduction of a discrete sliding step  $L/N$  results in a step width of the order parameter of  $\Delta\eta \approx 1/N$ . This explains the steps that are seen in Figs. 10(a,b). We conclude that only for a chain with infinitely many discretization points will a continuous transition look really continuous, whereas the chain with a finite number of discretization points will show a sequence of small but finite steps. In discriminating continuous from discontinuous transitions, i.e., in locating the tricritical point, this has to be taken into consideration. On the other hand, a genuinely discontinuous transition, as shown in Fig. 10(c), jumps from a symmetric to a highly asymmetric state in one step. No intermediate states can be generated, and discretization effects play no role.

We stress that we are extrapolating our results for a discrete model to the continuum limit, by a careful consideration of discretization effects (see Appendix B). It should be clear that of course all charged polymers and DNA, in particular, do indeed exhibit discrete charge distributions, and therefore the effects we see with our discrete model do re-

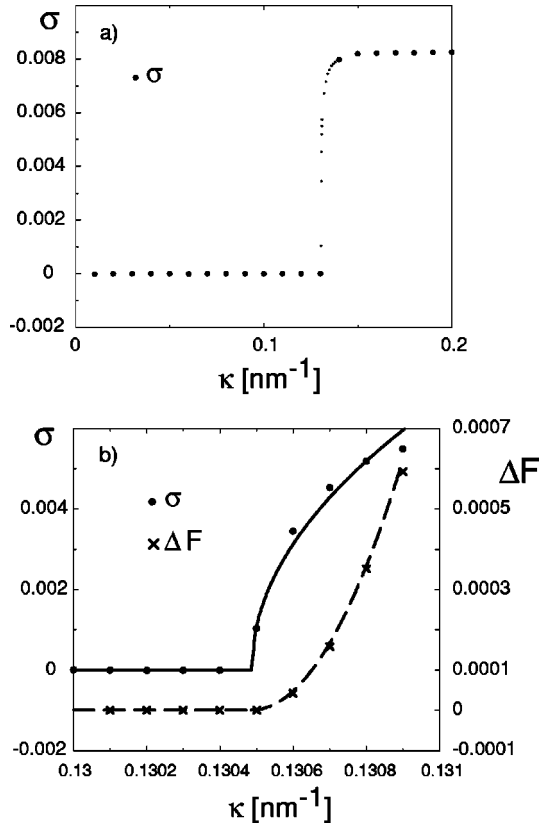


FIG. 12. Behavior of the mirror symmetry order parameter  $\sigma$  in the vicinity of the continuous phase transition from state III to state II at a sphere charge  $Z=40$  for a DNA strand of length  $L=50$  nm. (a) Every dot denotes the value of  $\sigma$  at the global minimum of Eq. (1) as a function of  $\kappa$ . Smaller dots are obtained for smaller step width ( $\Delta\kappa=10^{-4}$  nm $^{-1}$ ) in a sweep of the salt concentration. Intermediate points can be generated at will. The transition is continuous. (b) Comparison of the energy of the ground state configuration with a configuration that is constrained in a plane. The energy difference behaves as  $\Delta F \sim (\kappa - \kappa_c^2)$ , as denoted by the broken line, where  $\kappa_c = 0.130486$  nm $^{-1}$ . Positive  $\Delta F$  indicates that the 3D asymmetric state is favorable. For the order parameter  $\sigma$  we find  $\sigma \sim \sqrt{\kappa - \kappa_c}$ , solid line.

fect a property of real systems. However, the location of DNA charges with respect to the histone (which itself is only approximately described by a sphere) is by far not clear. Furthermore, the charges are not attached to the central line of the DNA but at the phosphodiester backbone. This leads to different discretization patterns than in our model. We therefore decided to concentrate on the continuum model as the limiting case of our discrete calculations. Nevertheless, as our investigations show, shape transitions that are predicted to be of second-order in the continuous limit can be transformed into first-order transitions as the discreteness of the charge distributions becomes pronounced.

We now examine the transition from symmetry class III to class II, i.e., the breaking of the mirror symmetry, the middle line in Fig. 9(b). The breaking of the mirror symmetry is a second-order transition. In Fig. 12(a) we present the order parameter behavior close to the transition for fixed sphere

charge  $Z=40$ , which is the same data as already shown in Fig. 8. In Fig. 12(b) we show the same order parameter at a smaller scale, where the continuous (but nonanalytic) behavior at the transition is clearly demonstrated. This transition is not distorted by discretization effects, because the arm that breaks the symmetry moves perpendicular to oscillations of the potential generated by the discrete charges on the DNA, see Figs. 6(c) and 6(d). Technically, this fact manifests itself through the absence of any metastable states. To establish the order of the transition precisely, we generate a sequence of two-dimensional reference configurations, which satisfy the constraint  $\sigma=0$  exactly. The energy difference between the optimal configuration, which breaks the mirror symmetry, and the reference configuration, which satisfies mirror symmetry, is denoted by  $\Delta F$  and plotted in Fig. 12(b) close to the transition. The energy difference  $\Delta F$  can be fitted with a quadratic function, while the order parameter can be fitted with a square root function, as one would expect for a standard continuous transition within a mean-field description. This establishes that the transition between symmetry classes III and II is indeed a continuous one.

The precise location of all three transition lines that are present at large salt concentrations (IV/III, III/II, and II/I) can only be determined for  $0 \text{ nm}^{-1} \leq \kappa < 3 \text{ nm}^{-1}$ , because the numerical minimization becomes increasingly difficult at high salt concentrations due to the strong screening of electrostatic interactions. For high  $\kappa$ , the energies of different configurations are very close. Although we cannot resolve the three transition lines (IV/III, III/II, and II/I), which get very close at high salt, we still can give the point of intersection between the phase IV (expanded) solution and the phase I (wrapped) solution. This transition is of first order. In Fig. 13 we show the energies of the symmetry states I and IV for  $Z=40$  and  $Z=70$ . As one can see, the energies cross with a finite angle, indicative of a discontinuous transition. As explained before, this high salt transition can be obtained by balancing the mechanical bending energy per unit length,  $F_{\text{bend}} = l_0/2R$ , and the local electrostatic DNA-sphere attraction,  $F_{\text{att}} = -Z\tau l_B/\kappa R^2$ , leading to the prediction for the transition value of the inverse screening length,  $\kappa_{\text{wrap}} = 2Z\tau l_B/l_0$ . For  $Z=40$ ,  $\kappa_{\text{wrap}} = 10.9 \text{ nm}^{-1}$  and for  $Z=70$ ,  $\kappa_{\text{wrap}} = 19.2 \text{ nm}^{-1}$ , which is quite close to the values seen in the numerical minimization. Taking into consideration the numerical error in calculating the bending rigidity (see Appendix B) and deviations from the tightly wrapped configuration in the numerical investigation, since parts of the DNA ends are released, the agreement is very good.

## V. RENORMALIZED DNA CHARGE

In the preceding section we neglected any nonlinear effects pertaining to the coion and counterion distributions around the sphere and DNA and treated all electrostatic interactions on the linearized Debye-Hückel level. The purpose of this section is to show to what extent the results change, if we include the effects of Manning condensation by renormalizing the DNA charge. We therefore repeated the numerical analysis of the phase diagram with a renormalized linear

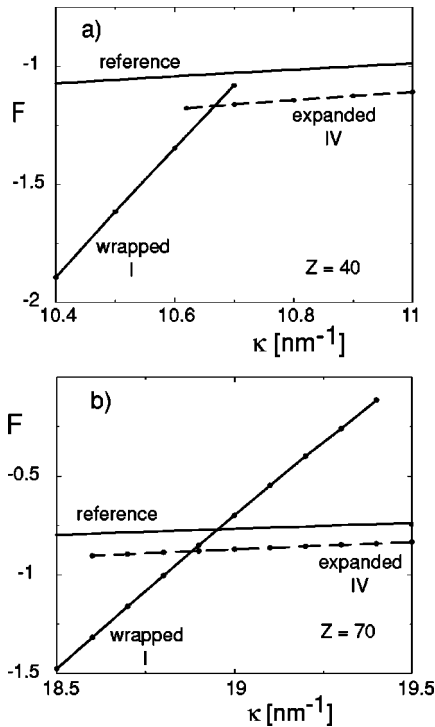


FIG. 13. Dewrapping transition for a DNA strand of length  $L = 50$  nm at high  $\kappa$  for  $Z=40$  (a) and  $Z=70$  (b). The energy of the equilibrium configurations vs inverse screening length  $\kappa$  is shown. Every dot denotes an equilibrated configuration which is not necessarily the ground state configuration. Lines are guides to the eye. The energy in the expanded state is less sensitive to  $\kappa$  variations than in the wrapped state. The discontinuous phase transition occurs where the energies cross. The reference state is a straight chain touching the sphere at half length and is added for comparison.

charge density of  $\tau=1/l_B$ , which is about a quarter of the bare linear charge density considered before. The main idea behind this charge renormalization is that counterions will strongly bind to the DNA and therefore reduce the effective line charge density [99]. We will at the end of this section discuss the limitations of this approach. Also, since the surface charge density of the histone equals the DNA surface charge density only for sphere charge of  $Z \approx 200$ , we can for the most part of the phase diagram neglect counterion condensation on the sphere.

In Fig. 14 we show the global phase diagram for a DNA strand of length  $L=50$  nm and with renormalized line charge density  $\tau=1/l_B$ . Comparison with the analogous phase diagram for the bare value of the DNA linear charge density in Fig. 9 demonstrates that no qualitative changes of the phase diagram topology are induced by reducing the linear charge density of the DNA. All four phases are present and are broken independently. The line indicating the boundary of the fully wrapped state ( $\eta=0, \sigma \neq 0$ , phase I) intersects the  $z$  axis ( $\kappa=0$ ) at  $Z=27.75$  (roughly a quarter of the value found for fully dissociated DNA). Since the total charge on the DNA is roughly 75, this results in a zero-salt overcharging of about 1.5 times the sphere charge. The transition line decreases to a minimum at  $\kappa \approx 0.5$  nm $^{-1}$ ,  $Z$

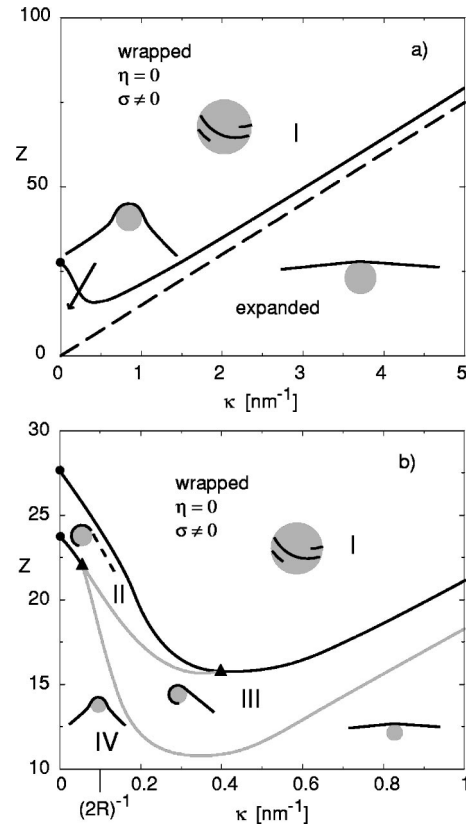


FIG. 14. Phase diagram for a DNA strand of length  $L = 50$  nm with a renormalized line charge density  $\tau=1/l_B$  as a function of sphere charge  $Z$  and inverse screening length  $\kappa$ . (a) The solid line indicates the boundary of the wrapped state ( $\eta=0, \sigma \neq 0$ ; phase I). The minimal sphere charge to wrap the DNA occurs at  $\kappa^{-1} \approx 0.5$  nm (25 mM). The dashed line is the local-energy-balance argument for the wrapping transition. (b) Detail of phase diagram for small  $\kappa$ , featuring all four different phases. Discontinuous (continuous) transitions are denoted by black (gray) solid lines.

$\approx 11$ , then increases with  $\kappa$  and approaches the prediction from the local-energy-balance argument, see broken line in Fig. 14(a). The high- $\kappa$  slope of the lines is about four times larger than in the unrenormalized case considered before. In Fig. 14(b) we show an enlarged view of the low- $\kappa$  region with all phase transitions. The bottom line denotes the transition from the expanded state ( $\eta=0, \sigma=0$ ; phase IV) to the 2D asymmetric state ( $\eta \neq 0, \sigma=0$ ; phase III). In contrast to our findings in the preceding section, this transition does not exhibit a tricritical point, the transition is always continuous and terminates at a critical end point at  $Z=22$  and  $\kappa = 0.055$  nm $^{-1}$  (left triangle). The middle line denotes the transition between the 2D asymmetric state ( $\eta \neq 0, \sigma=0$ ; phase III) and the 3D asymmetric state ( $\eta \neq 0, \sigma \neq 0$ ; phase II); the transition is of second order. As opposed to the line found in the preceding section this line now has two critical end points. The first critical end point coincides with that for the bottom line and forms a bicritical point ( $Z=22$  and  $\kappa = 0.055$  nm $^{-1}$ ). The second one occurs at  $Z=15.75$  and  $\kappa = 0.4$  nm $^{-1}$ . Above the bicritical point at  $Z=22$  and  $\kappa = 0.055$  nm $^{-1}$ , the solid black line denotes a direct first-

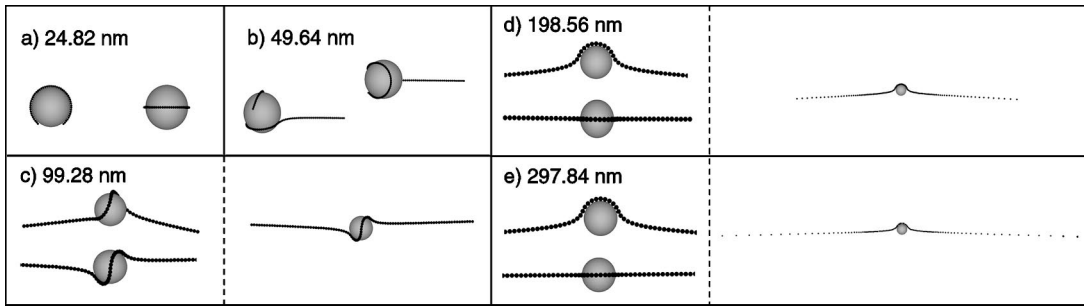


FIG. 15. DNA conformations at a fixed sphere charge  $Z=100$  in the absence of salt for varying chain length, (a) 73 base pairs,  $L=24.82$  nm, (b) 146 base pairs  $L=49.64$  nm, (c) 292 base pairs,  $L=99.28$  nm, (d) 584 base pairs,  $L=198.56$  nm, and (e) 876 base pairs,  $L=297.84$  nm. For each length we show the DNA configuration on an identical scale, for configurations (c)–(e) we also include pictures that contain the complete chain. In (b) and (c) the mirror symmetry is broken, in (a), (d), and (e) it is conserved. The length of the chain that touches the sphere decreases as the chain length increases, since the DNA arms pull the center segment flat due to their mutual repulsion. In (d) and (e) we used a variable discretization.

order transition between the expanded state ( $\eta=0$ ,  $\sigma=0$ ; phase IV) and the 3D asymmetric state ( $\eta\neq 0$ ,  $\sigma\neq 0$ ; phase II). This line ends at  $Z=23.75$  and  $\kappa=0$  (lower solid circle). The upper line is the same line as the one drawn in Fig. 14(a) and denotes the boundary of the fully wrapped state ( $\eta=0$ ,  $\sigma\neq 0$ , phase I). As demonstrated in detail before, we infer the order of all transitions from the behavior of the order parameter and the energy difference. In summary, we found that the qualitative aspect of the phase diagram is left unchanged by Manning condensation. However, some details and the precise location of phase transitions are sensitive to this effect.

We hasten to add that the simple procedure of replacing the bare line charge density of the DNA by the renormalized one is a crude approximation for the following two reasons:

(i) Even for a straight charged polymer in the absence of an oppositely charged sphere, the charge-renormalization procedure is only valid for a finite window of low but not too low salt concentrations. At zero salt concentration and vanishing histone concentration, no counterions can condense on the DNA (since it is an object of finite extent) and the Coulomb limit of Fig. 9 is recovered characterized by the bare DNA line charge density. Also at high enough salt concentrations the Debye-Hückel theory becomes valid even for highly charged cylinders with  $\tau l_B > 1$ : A simple box model for the counterion distribution around the cylinder [111] suggests that for salt concentrations  $\kappa R > \tau l_B$ , the surface potential is correctly given by the DH theory and thus the bare linear charge density has to be used in the free energy expression Eq. (1).

(ii) If two oppositely charged objects, each with a layer of condensed ions, approach, pairs of condensed ions are jointly released into the solution. This effect has been recently numerically studied within the full Poisson-Boltzmann approach for the case of a cylinder at a planar charged surface [102]. It was found that ions are locally released in the region of contact, which makes the analytical prediction of such effects difficult. Solving the present problem of a deformable charged cylinder at an oppositely charged sphere within the full PB scheme is desirable but numerically not possible. The phase diagram obtained in this section should therefore only

be considered as an estimate of the maximally possible effect that charge renormalization can have.

## VI. VARIATION OF DNA LENGTH

So far we have considered a DNA strand of fixed length  $L=50$  nm, corresponding to a nucleosomal core particle with 146 base pairs. In this section we investigate effects due to a varying DNA length, as they occur, for example, for chromatosomal particles for different digestion strengths. Another example where such effects could be studied are of course reconstituted nucleosomal particles with synthetic DNA strands of fixed and rather arbitrary length.

As an illustration of how DNA length modifies the complexation behavior, consider Fig. 15 where equilibrium DNA structures for a fixed sphere charge  $Z=100$ , full DNA charge density  $\tau=2/0.34$  nm, and varying chain length at zero salt are shown. For very short strands, see (a), the DNA is fully wrapped around the sphere. Short DNA chains exhibit the 3D asymmetric state II, the single arm configuration, see (b), while longer DNA chains are organized in a configuration with two DNA arms of almost equal length, see (c). The mirror symmetry is restored for very long chains, see (d) and (e). This sequence of transitions has already been discussed by Mateescu *et al.* [25]. It is clear that the amount of wrapping (the meaning of this term will be precised below) first increases and then decreases as a function of length, the latter trend can be easily understood as a result of the electrostatic repulsion between the two extending DNA arms, as will be discussed shortly.

The effect of DNA length on the phase diagram is illustrated in Fig. 16, where we show the wrapping transition from state I to state II for a DNA length of  $L=50$  nm (already shown in Fig. 9) and for a length  $L=70$  nm. The transitions between states II, III, and IV are not shown. The former length corresponds to a fully digested nucleosomal core particle, while the latter length might be more representative of DNA at the initial stage of digestion, where some of the linker DNA is retained on the histone particle. It is seen that at increasing chain length the transition moves to higher values of the sphere charge, or, at constant histone charge,

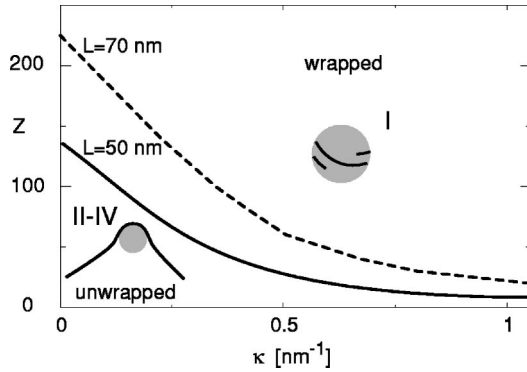


FIG. 16. Phase transition from the wrapped state ( $\eta=0$ ,  $\sigma\neq 0$ , phase I) to the 3D asymmetric state ( $\eta\neq 0$ ,  $\sigma\neq 0$ , phase II) for two different DNA lengths. The solid line denotes the fully digested nucleosomal core DNA of length  $L=50$  nm and the dashed line represents the transition for DNA of length  $L=70$  nm, which corresponds to the nucleosomal core DNA plus linker DNA.

the transition moves to larger salt concentrations. It is noteworthy that indeed the influence of different DNA lengths on the low salt nucleosomal stability threshold has been extensively discussed in the experimental community [72].

To get a simple yet quantitative description of the dependence of the amount of wrapped DNA on the DNA length, we repeat here an argument initially made for the salt dependence of the low-salt unwrapping transition for an infinite charged polymer chain [23]. As a result, we will obtain the critical sphere charge which is needed to wrap a certain length  $X$  of DNA around the charged sphere.

For our calculation we compare the Coulomb energies in the reference state depicted in Fig. 17(a), where the DNA is straight and touches the sphere only at one point, and in the wrapped state Fig. 17(b), where a segment of length  $X$  is wrapped around the sphere. We assume that the sphere in the wrapped state is positioned in the middle of the nonwrapped DNA portion, as indeed is obtained for very long DNA chains, see Fig. 15. Our results are therefore valid only for rather long chains. More detailed models have been devised for the one-tail configuration, which is important when the DNA is short enough that it is almost completely wrapped around the sphere [25]. We also do not treat the charge distribution of the DNA in the wrapped region very carefully and assume that it forms one or multiple circles. Models treating the correlation effects of the wrapped part carefully have been considered recently [26].

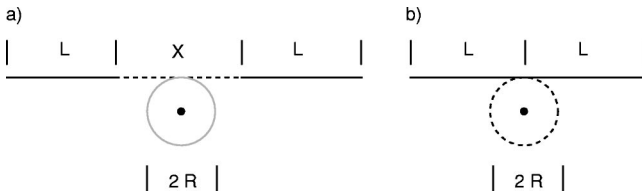


FIG. 17. The two DNA conformations that are compared in the scaling argument for the length dependence of the wrapping transition. (a) Straight chain touching sphere at one point. (b) The DNA segment of length  $X$  (drawn as broken line) is wrapped around the sphere.

Four contributions determine the energy difference which in the following we discuss one by one.

(i) The two solid straight lines in (a) separated by a distance  $X$ , the electrostatic energy is (for zero salt) given by

$$\begin{aligned} E_i^a &= \tau^2 l_B \int_0^L ds \int_0^L ds' \frac{1}{s+s'+X} \\ &= \tau^2 l_B [X \ln X + (2L+X) \ln(2L+X) \\ &\quad - 2(L+X) \ln(L+X)]. \end{aligned} \quad (5)$$

The interaction between the two solid lines in configuration (b) is given by

$$E_i^b = \tau^2 l_B \int_0^L ds \int_0^L ds' \frac{1}{s+s'} = 2\tau^2 l_B L \ln 2. \quad (6)$$

The energy difference between the configurations is in the limit  $L/X \rightarrow \infty$  given by

$$\Delta E_i = E_i^b - E_i^a \approx \tau^2 l_B X \ln(L/X) \quad (7)$$

and thus diverges logarithmically as the DNA arms become longer. We will later see that this is in fact the driving force for the gradual unwinding of the DNA from the sphere seen in Fig. 15 as the DNA length increases.

(ii) The straight lines interact with the dashed line differently in configurations (a) and (b). The interaction in (a) is

$$\begin{aligned} E_{ii}^a &= 2\tau^2 l_B \int_0^L ds \int_0^X ds' \frac{1}{s+s'} \\ &= 2\tau^2 l_B [L \ln(1+X/L) + X \ln(1+L/X)]. \end{aligned} \quad (8)$$

The calculation of the interaction between the DNA segment drawn as a broken line in configuration (b), which we envision to be wrapped in one or several circles around the sphere of radius  $R$ , depending on the length  $X$ , and the straight strands (drawn as solid lines), is more complicated. Since we are interested in effects as the arms become very long, the specific details of the charge distribution do not matter much and we can treat the charge of the wrapped DNA portion as being replaced by a point charge of magnitude  $X\tau$  located in the sphere center. With this simplification the interaction with both straight DNA arms becomes

$$\begin{aligned} E_{ii}^b &= 2\tau^2 l_B \int_0^L ds \frac{X}{\sqrt{R^2+s^2}} \\ &= 2\tau^2 l_B X \ln(L/R + \sqrt{L^2/R^2+1}). \end{aligned} \quad (9)$$

The energy difference is finite in the limit of  $L/X \rightarrow \infty$  and  $L/R \rightarrow \infty$  and is given by

$$\Delta E_{ii} = E_{ii}^b - E_{ii}^a \approx \tau^2 l_B X \ln(X^2/R^2). \quad (10)$$

(iii) The difference of self-interaction of the dashed line in configurations (a) and (b) reads,

$$\Delta E_{iii} \sim \tau^2 l_B X \quad (11)$$

as follows from our detailed calculation in Appendix A and therefore constitutes an unimportant constant.

(iv) The difference of the attraction between the DNA and the sphere is in the limit of very long DNA strand given by

$$\Delta E_{iv} \approx -Z\tau l_B 2\pi X/R \quad (12)$$

and simply corresponds to the Coulomb energy of two charges of  $Z$  and  $2\pi\tau X$  at a mutual distance  $R$ .

Adding up the energy difference contributions in Eqs. (7), (10), and (12), we arrive at the total energy difference

$$\Delta E \approx -Z\tau l_B 2\pi X/R + X\tau^2 l_B \ln(XL/R^2). \quad (13)$$

When this energy difference is zero, the wrapped and unwrapped configurations are of equal energy, which corresponds to a wrapping transition. The critical charge where this happens, denoted by  $Z^*$ , is

$$Z^* \sim \tau R \ln\left(\frac{LX}{R^2}\right). \quad (14)$$

As a main result, the critical sphere charge needed to wrap a DNA strand of length  $X$  around the sphere increases logarithmically with the strand length  $X$ , but also with the DNA length  $L$ .

We now show a numerical corroboration of this result for a DNA strand of nominal charge density  $\tau = 2/0.34$  nm. For the numerical analysis, we need to define when we consider a DNA segment as being wrapped precisely, which, of course, introduces a certain arbitrariness into the result. We call a DNA monomer wrapped when it is contained within a spherical shell of thickness  $D$  around the sphere representing the histone protein. In the following, we show that the results are robust with respect to variation of the free parameter  $D$  within a sensible range of parameters. The DNA length ranges between 100 nm and 1000 nm. In our actual numerical calculations we determine the equilibrium DNA configuration for fixed sphere charge and DNA length and from that deduce the length of the wrapped DNA portion. In Fig. 18 we plot the critical sphere charge  $Z^*$  as a function of the DNA length  $L$  on a logarithmic scale. The behavior follows a straight line, confirming the prediction Eq. (14). It is also seen that the precise value of the shell thickness  $D$  used to distinguish wrapped DNA from unwrapped DNA is unimportant unless one is interested in obtaining numerical prefactors.

In Figs. 19 and 20 we show the amount of wrapped DNA  $U = \tau X$  as a function of the DNA length  $L$  and as a function of the sphere charge  $Z$ . Each figure brings out different aspects of the wrapping behavior at vanishing salt concentration. In both figures the spherical shell used to determine the amount of wrapped DNA has a thickness of  $D = 1$  nm. The main point of Fig. 19 is the continuous crossover from overcharging of the sphere (the amount of wrapped DNA which exactly neutralizes the sphere charge is denoted by a broken line for each of the four different data sets) to undercharging of the sphere, which is located at the point where the data

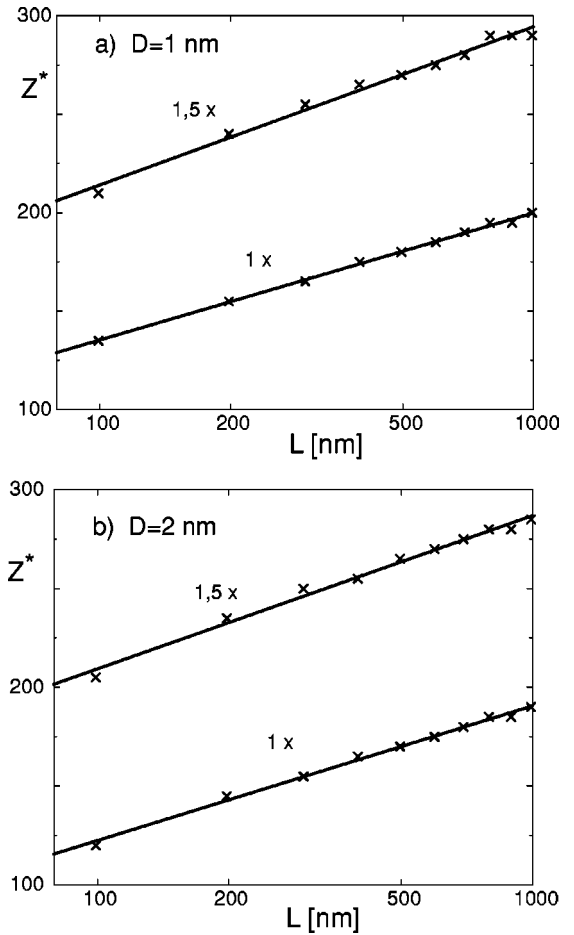


FIG. 18. Critical sphere charge needed to wrap the chain once (corresponding to a strand of length  $X = 31$  nm) and 1.5 times (corresponding to a length  $X = 47$  nm) around the sphere as a function of the total chain length  $L$ . In (a) a DNA monomer is considered wrapped when it is found within a shell of thickness  $D = 1$  nm around the sphere, in (b) we show results for  $D = 2$  nm. The dependence on the chain length is well described by a logarithm (solid lines).

cross the broken lines. The DNA length where this crossover occurs moves out to larger lengths as the sphere charge increases. This sheds some light on the transition from a symmetric configuration with two DNA arms of roughly equal length, which occurs for long DNA, to the asymmetric configuration with only a single DNA arm, as observed in the configurations shown in Fig. 15. This can be rationalized because for long DNA arms the complex becomes undercharged, and therefore there is a net attraction between the complex and the dangling DNA arms, pulling the complex into the middle of the DNA arms, while for short DNA arms the complex becomes overcharged, giving rise to a net repulsion between the complex and the DNA arms, pushing the complex to the extremity of the noncomplexed DNA [26].

Figure 20 visualizes the symmetry-breaking transition from a planar DNA configuration, at very low sphere charge, to a three-dimensional configuration. This transition, which roughly occurs at a constant amount of wrapped DNA, moves out to larger sphere charge as the DNA becomes

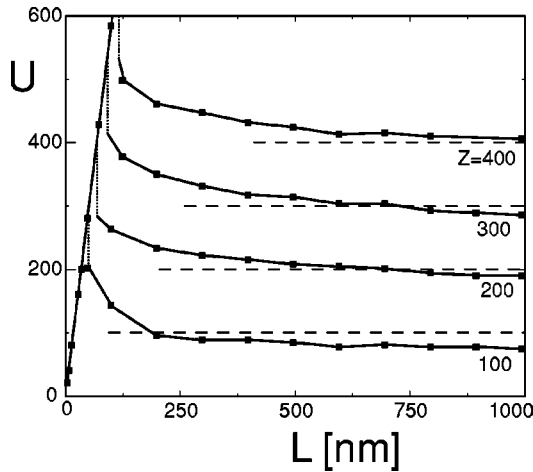


FIG. 19. Wrapped DNA charge  $U$  versus DNA length  $L$  for four fixed sphere charges ( $Z = 100, 200, 300, 400$ ) in the absence of salt. One full turn corresponds to a wrapped charge of  $U = 184.4$ . For small chain lengths, all data collapse onto a single straight line corresponding to completely wrapped DNA, for larger  $L$  a discontinuous transition occurs (denoted by broken vertical lines) and part of the DNA unwraps. For very large  $L$  the wrapped charge becomes less than that needed to neutralize the sphere charge (denoted by horizontal broken lines).

longer, in agreement with our analytical arguments leading to Eq. (14). This transition is denoted by a broken line in Fig. 20 and it occurs at a wrapped charge which corresponds to almost a full turn of wrapped DNA. This is in agreement with the configurations shown in Fig. 15 for a fixed sphere charge  $Z = 100$ , where the DNA chains longer than  $L = 100$  nm show a two-dimensional structure whereas shorter chains exhibit a three-dimensional structure. The crossover indeed occurs where roughly one turn of DNA is wrapped around the sphere.

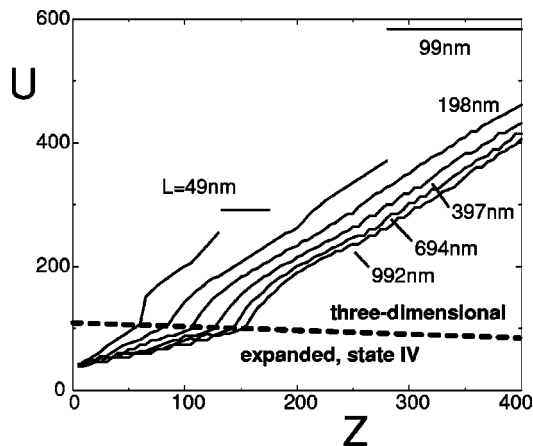


FIG. 20. Wrapped DNA charge  $U$  versus sphere charge  $Z$  for six fixed chain lengths (146 BP  $\sim L = 49.6$  nm, 292 BP  $\sim L = 99.28$  nm, 584 BP  $\sim L = 198.56$  nm, 1168 BP  $\sim L = 397.12$  nm, 2044 BP  $\sim L = 694.96$  nm, 2920 BP  $\sim L = 992.8$  nm) in the absence of salt. The broken line denotes the transition between the planar two-dimensional configuration (for small  $U$ ) and a configuration where the mirror symmetry is broken. The jump at large values of  $Z$  is the transition to the fully wrapped configuration.

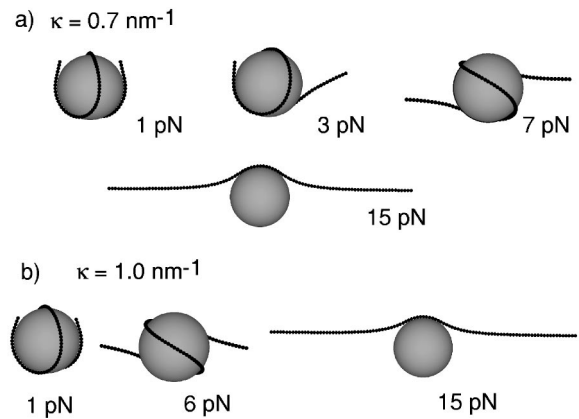


FIG. 21. Equilibrium DNA configurations for a DNA strand of length  $L = 50$  nm and sphere charge  $Z = 20$  for various representative external forces  $f$ . (a) Configurations are shown for salt concentration of  $\kappa = 0.7$  nm $^{-1}$ ; at an intermediate force of  $f = 3$  pN a configuration appears which breaks the twofold rotational symmetry. At large force  $f = 15$  pN the DNA is in the expanded state IV. (b) Configuration for slightly higher salt concentration  $\kappa = 1.0$  nm $^{-1}$ .

For finite salt concentration, the DNA length  $L$  has to be replaced by the screening length  $\kappa^{-1}$  whenever the screening length is smaller than the DNA length. This leads to the salt dependence of the wrapping transition at low salt concentrations, as discussed previously [23].

### VII. STRETCHING FORCE

Very recently, a number of experiments have been reported where nucleosomal structures have been subjected to externally applied forces and the resulting DNA extension has been measured [59,60]. In those experiments, the DNA was typically quite long, and a whole lot of histone proteins were attached to the chain. In such experiments there is a dynamic equilibrium between histones attached to the DNA and histone detached from the DNA, including interactions between histones on the DNA. As one of the main findings, the response of chromatin to applied force depends on the salt concentration. In this section, we show how the DNA conformation of a single strand of length  $L = 50$  nm changes as an external stretching force is applied to the two ends. Our model neglects many of the effects present in the experiments [59,60], most notably the interaction between different nucleosomes. However, it seems that our model captures some of the salient features seen in experiments, as will be explained at the end of this section.

Within our microscopic model defined by the free energy expression Eq. (1), an external force couples to the two ends of the DNA. We therefore have to minimize the modified free energy expression

$$F_{\text{force}} = F - \mathbf{f} \cdot [\mathbf{r}(L) - \mathbf{r}(0)] / k_B T, \quad (15)$$

where  $F$  denotes the free energy functional Eq. (1) and the force  $\mathbf{f}$  points into an arbitrary direction.

In Fig. 21 we show representative equilibrium configura-

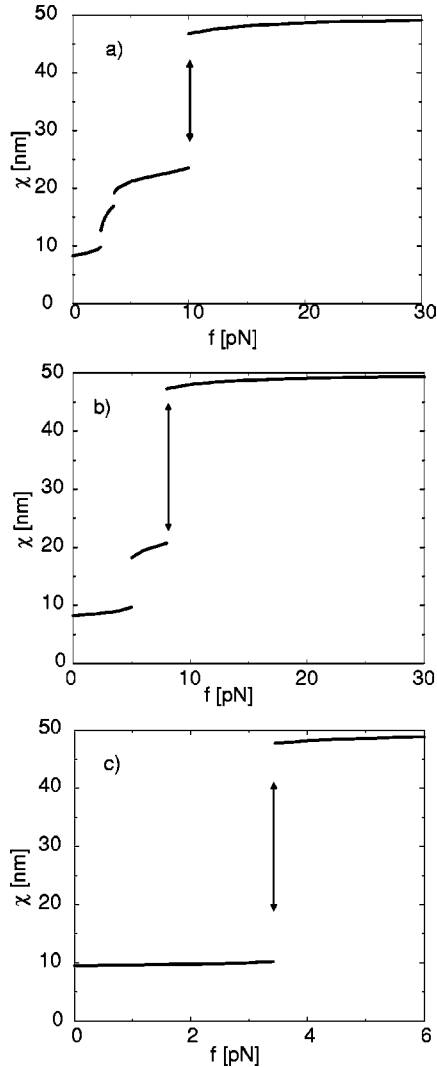


FIG. 22. Chain extension  $\chi$  for a sphere charge  $Z=20$  as a function of the external force for three different values of the salt concentration (a)  $\kappa=0.7 \text{ nm}^{-1}$ , (b)  $\kappa=1.0 \text{ nm}^{-1}$ , and (c)  $\kappa=2.0 \text{ nm}^{-1}$ . It is seen that the discontinuity of the stretching response gets more pronounced with increasing salt concentration. Furthermore, the rotationally asymmetric configuration seen in (a) [cf. Fig. 21(a), 3 pN] is absent in (b) and (c).

tions obtained by minimizing the functional Eq. (15) for a sphere charge  $Z=20$ . At the lower salt concentration,  $\kappa=0.7 \text{ nm}^{-1}$ , depicted in Fig. 21(a), several different symmetries are observed as the applied force increases. For a force of  $f=1 \text{ pN}$  the complex is in state I, which is also realized in the absence of an external force; for a somewhat higher force of  $f=3 \text{ pN}$ , state II is realized, while for a slightly higher force at  $f=7 \text{ pN}$  the complex jumps back to state I. For an even higher force of  $f=15 \text{ pN}$  the force has destroyed the wrapped state and induced the expanded state. Somewhat similar behavior is observed at a higher salt concentration of  $\kappa=1.0 \text{ nm}^{-1}$ , depicted in Fig. 21(b). In contrast to the lower salt concentration, we do not observe state II at intermediate forces in Fig. 21(b).

To quantify our results, we introduce the parameter

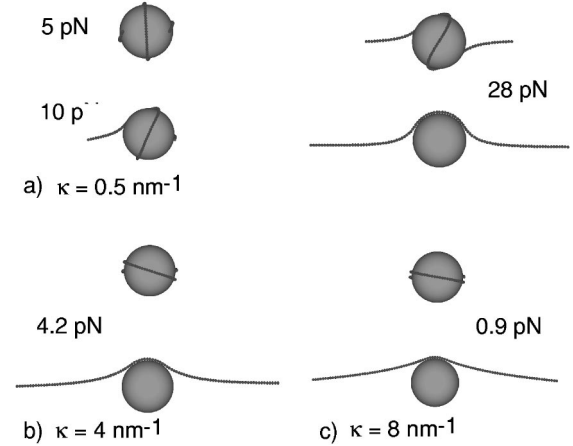


FIG. 23. DNA configurations for a sphere charge  $Z=40$ . (a) For low salt concentration  $\kappa=0.5 \text{ nm}^{-1}$ , at  $f=5 \text{ pN}$  the complex is only weakly affected by the external force. At  $f=10 \text{ pN}$  one arm is pulled out (rotational symmetry broken). At  $f=28 \text{ pN}$ , the rotationally symmetric, mirror symmetric complex undergoes a discontinuous transition to the extended state. (b) At high salt concentration,  $\kappa=4 \text{ nm}^{-1}$ , all intermediate steps have vanished: The complex stays unaffected in the complexed conformation until it almost completely expands in a discontinuous transition at a plateau force  $f=4.2 \text{ pN}$ . (c) At even higher salt concentration,  $\kappa=8 \text{ nm}^{-1}$ , the plateau force has decreased to  $f=0.9 \text{ pN}$ .

$$\chi = \sqrt{[\mathbf{r}(0) - \mathbf{r}(L)]^2}, \quad (16)$$

which measures the spatial extension (or end-to-end distance) of the DNA chain. This parameter is plotted in Fig. 22 for  $Z=20$  and three different salt concentrations. For all three salt concentrations the extension parameter  $\chi$  starts, for vanishing force, at about  $\chi=10 \text{ nm}$ , which corresponds to the fully wrapped state, and approaches  $\chi=50 \text{ nm}$ , the contour length of the DNA strand, for high forces. The situation at low salt is depicted in Fig. 22(a). One discerns two discontinuous transitions at  $f=2.5 \text{ pN}$  and  $f=3.5 \text{ pN}$ , between which the DNA is in a rotationally asymmetric configuration, compare Fig. 21(a). At a higher force of about  $10 \text{ pN}$  a rather large discontinuity appears, where the chain extension roughly doubles. At slightly larger salt concentration, Fig. 22(b), the intermediate state II has disappeared, and a discontinuous transition at  $f=5 \text{ pN}$  between two states I with different values of the extension parameter is seen. At a larger force of  $f=8 \text{ pN}$  a strongly discontinuous transition appears between the wrapped and the expanded phases, states I and IV. At even larger salt concentration, Fig. 22(c), only a single transition is left at which the configuration jumps from the fully wrapped to the fully expanded state. Our results for the two different salt concentrations in Figs. 22(b) and 22(c) entail the presence of a critical point at intermediate salt concentrations. As the main result, it is seen that at large salt concentration, the force response consists of a single jump at a certain plateau force, whereas at low salt concentrations the extension grows rather continuously at low forces. This continuous growth can be understood as being due to electrostatic repulsion between DNA segments,

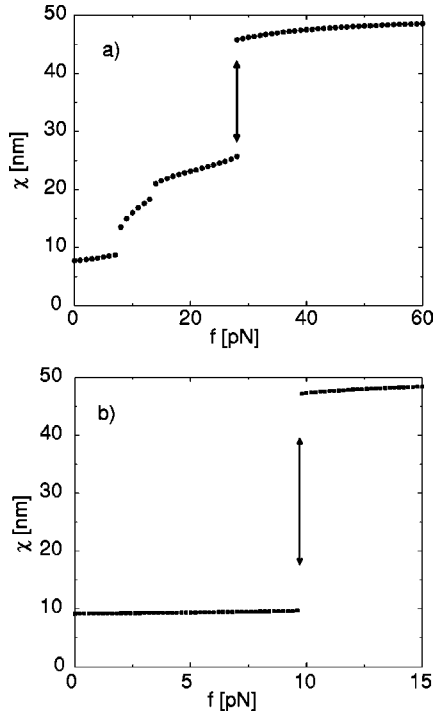


FIG. 24. DNA extension as a function of the externally applied stress for a sphere charge  $Z=40$ . (a)  $\kappa=0.5 \text{ nm}^{-1}$  (b)  $\kappa=2 \text{ nm}^{-1}$ .

which gradually assist the external force in detaching the DNA from the sphere. For larger salt concentration, on the other hand, the wrapping state can be understood by a simple local-energy argument, as will be explained in more detail later on. This qualitative difference between the force response at low and high salt concentrations is in agreement with experimental results, where a force plateau could only be observed at high salt concentrations whereas at low salt concentrations the extension rose continuously as the force was increased [59].

In Fig. 23 we show some configurations obtained for a higher sphere charge  $Z=40$ . At low salt conditions,  $\kappa=0.5 \text{ nm}^{-1}$ , depicted in Fig. 23(a), the dewrapping with increasing force occurs in several steps, similar to our results for sphere charge  $Z=20$ . First, one arm is pulled out (depicted configuration at  $f=10 \text{ pN}$ ), making the complex totally asymmetric ( $\eta \neq 0, \sigma \neq 0$ ; phase II). Then, at higher force, the second arm is pulled out and at even higher force,  $f=28 \text{ pN}$ , a highly discontinuous transition to the fully extended state occurs. The corresponding force is called plateau force and in Fig. 23(a) we show the two coexisting configurations. In Fig. 23(b) we show the completely different situation for high salt ( $\kappa=4 \text{ nm}^{-1}$ ). Here, for  $f < 4.2 \text{ pN}$  no structural changes are induced in the complex. At  $f=4.2 \text{ pN}$  the complex expands directly and highly discontinuously to the almost fully expanded state. At still higher salt concentrations,  $\kappa=6 \text{ nm}^{-1}$ , the same behavior is observed. In Figs. 23(b) and 23(c) we show the coexisting states at this force-induced dewrapping transition.

The extension parameter is plotted in Fig. 24 for  $Z=40$  and two salt concentrations which exemplify the behavior at

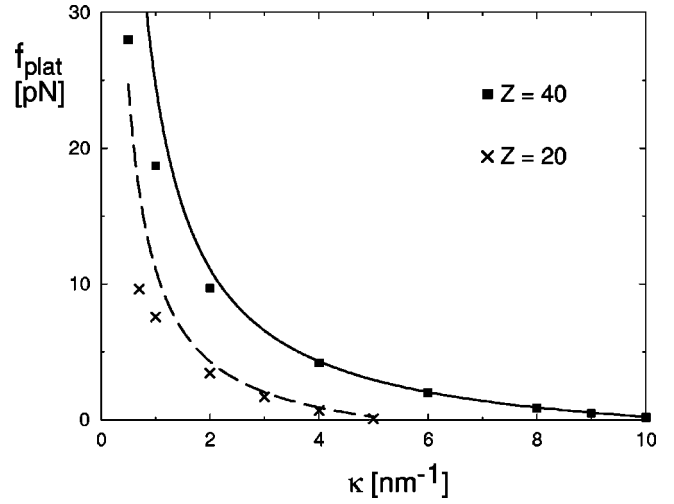


FIG. 25. Plateau force  $f_{plat}$  versus inverse screening length  $\kappa$  for sphere charges  $Z=20$  and  $Z=40$ . Crosses (squares) denote numerical results for  $Z=20$  ( $Z=40$ ). The dashed (solid) line denotes analytic results for  $Z=20$  ( $Z=40$ ) according to Eq. (18). Above  $\kappa \approx 2 \text{ nm}^{-1}$ , numerical and analytical calculations agree well. The curves predict a vanishing plateau force at  $\kappa=5.5 \text{ nm}^{-1}$  ( $Z=20$ ) and  $\kappa=11 \text{ nm}^{-1}$  ( $Z=40$ ), which reflects the presence of the salt-induced dewrapping transition.

low- and high-salt conditions. The situation at low salt is depicted in Fig. 24(a). Between the two discontinuous transitions at  $f=8 \text{ pN}$  and  $f=14 \text{ pN}$ , the twofold rotational symmetry is broken, while at a larger force of  $f=28 \text{ pN}$  a strongly discontinuous transition from the wrapped phase ( $\eta=0, \sigma \neq 0$ ; phase I) to the expanded phase ( $\eta=0, \sigma=0$ ; phase IV) occurs. This sequence of symmetries is the same as for sphere charge  $Z=20$ . The situation at high salt,  $\kappa=2 \text{ nm}^{-1}$ , is depicted in Fig. 24(b). Here, no intermediate phases are present and the system goes directly from the wrapped phase ( $\eta=0, \sigma \neq 0$ ; phase II) to the expanded phase ( $\eta=0, \sigma=0$ ; phase IV) at a plateau force of  $f=9.7 \text{ pN}$ .

At high-salt conditions, the asymptotic functional relation between the plateau force and the inverse screening length is simple. As screening is strong, nonlocal interactions can be neglected. Equating the energy of the fully expanded state, which only consists of the force-induced energy  $fL$ , with the energy of the fully wrapped state, which contains the electrostatic attraction and the mechanic bending energy (and neglecting the force contribution as the two ends are close by),

$$-\frac{|f_{plat}|L}{k_B T} = -\frac{Z\tau Ll_B}{\kappa R^2} + \frac{l_0 L}{2R^2}, \quad (17)$$

we obtain the plateau force  $f_{plat}$ . The thermal energy is  $k_B T = 4.1421 \text{ pN} \times \text{nN}$  at 300 K. Solving for  $f_{plat}$  we obtain

$$f_{plat} = k_B T \left( \frac{Z\tau l_B}{\kappa R^2} - \frac{l_0}{2R^2} \right). \quad (18)$$

For high  $\kappa$ , this agrees very well with numerical calculations, as is demonstrated in Fig. 25, where we show the numerically determined plateau forces (data points) for  $Z=20$ , 40 and compare them with the analytical prediction according to Eq. (18). Our analytic argument is based on a balance of local-energy contributions and therefore becomes invalid when nonlocal electrostatic interactions start to dominate. From Fig. 25 we see that this crossover occurs at about  $\kappa = 1 \text{ nm}^{-1}$  for our system. This also roughly is the threshold below which the extension behavior starts to be dominated by the continuous increase of the extension and where symmetry transitions occur at intermediate values of the applied force. Our results for the plateau force agree quite well with recent results from AFM experiments [59] (where the plateau force was found to be of the order of 5 pN for a salt concentration of the order of 100 mM) if one assumes that the effective histone charge can be represented by a value of  $Z = 20$ . This effective histone charge agrees roughly with our estimate from the critical salt concentrations at which the dewrapping transitions occur, see Sec. IV C. In a second experiment a somewhat higher value for the plateau force was obtained [60], but it is clear from our results that meaningful comparison between different experiments can only be done at identical salinity. Our results suggest that part of the stretching response of a chromatin fiber is due to internal rearrangements and interaction within a single nucleosomal particle and that the strain-stress relation of the nucleosomal subunit is an indispensable input for any serious mechanical model of the chromatin structure.

### VIII. CONCLUSION

In this paper we have considered the interaction of a semiflexible polyelectrolyte and an oppositely charged sphere with specific emphasis on the experimentally relevant DNA-histone system. We concentrated on the salt dependence of the resulting complex structure and investigated the influence of externally applied forces, DNA length variation, and DNA charge renormalization, using the DNA symmetry group as a means to classify its conformation.

For given linear charge density of the polyelectrolyte, the system exhibits two distinct responses to a variation of the ambient salt concentration, depending on the charge  $Z$  of the sphere. For  $Z < Z^*$ , where  $Z^*$  is a threshold charge, the polyelectrolyte exhibits a salt-dependent deflection towards the sphere, which is maximal for an intermediate salt concentration and disappears both for very small and very large salt concentrations. The polyelectrolyte is always described by a planar curve, i.e., it exhibits mirror and a twofold rotational symmetry. This case might be applicable to small basic proteins adsorbing onto DNA. For  $Z > Z^*$  the system assumes four different symmetry states, which are defined via the existence or nonexistence of the independent rotational and mirror symmetries. For very low and very high salt concentrations, the polyelectrolyte is in an extended conformation. The low-salt expansion occurs at a value of the screening length  $\kappa^{-1}$ , which is of the order of the sphere diameter. For intermediate salt concentrations, the polyelectrolyte is wrapped around the sphere. These results are in accord with

experimental findings concerning the stability of the nucleosomal core particle upon variations of the salt concentration of the solvent [84]. At high salt concentrations we find a dewrapping transition at an inverse screening length of  $\kappa_{\text{wrap}} \sim Z\tau$ . The linear dependence of  $\kappa$  on  $Z$  and  $\tau$  is in accord with experiments on synthetic systems [1,2].

According to our calculations, the sphere charge that accounts for the experimentally found conformational transitions of the nucleosome, i.e., salt concentrations of  $\approx 1 \text{ mM}$  and  $1 \text{ M}$ , range between  $Z=12$  (for fully charged DNA without taking into account counterion condensation) and  $Z=20$  (taking into account charge renormalization via DNA charge renormalization). This is in rough agreement with experiments of Khrapunov *et al.* The authors find that only about 30 of the 200 basic residues of the core histones are involved in interactions with DNA [79].

Our results also agree qualitatively with experiments in which the nucleosome is destabilized by heating the system [62,65]. Since  $\kappa \sim 1/\sqrt{T}$ , heating of the system leads to a decrease in  $\kappa$ , which results in an extended phase. It must be noted, however, that thermal denaturation affects many parameters of the system, and eventually leads to the melting of the DNA double strand structure, thus making a detailed comparison with our model impossible.

Increasing the DNA length results in a higher sphere charge that is needed to wrap the DNA. Formulated differently: The larger the stretches of uncomplexed DNA (e.g., linker DNA) the lower the stability of the core particle.

Our calculations in the presence of an applied external force show two distinct patterns of unfolding, depending on the salt concentration. At low salt concentrations, the polyelectrolyte gradually unfolds for increasing force and exhibits a sequence of all four symmetry states. At a certain force threshold, called the plateau force, the polyelectrolyte discontinuously expands to almost full length. At high salt concentration, no gradual unfolding occurs; at the plateau force the system directly expands from a wrapped to an almost fully expanded state. This is in good agreement with experiments on stretched chromatin fibers [59].

All our results demonstrate that indeed electrostatic forces play a dominant role in the formation of the DNA-histone complex. In a number of experiments on salt effects on nucleosomal core particle structures, the authors attributed different symmetry states of the nucleosome to different salt concentrations. Their strategy consisted of finding structural models for which the theoretically calculated scattering data [72] or hydrodynamic/optical data [70,71] coincides with experimentally obtained data. It would be interesting to redo such calculations with our conformations.

Useful extensions of our model would include the calculation of interactions between two or more nucleosomes. For high enough salt concentration, the chromatin structure switches from the extended bead-on-a-string structure to a fiber of 30 nm in diameter. This further step of DNA condensation must be the result of a net attraction between nucleosomes, which should naturally come out of such more detailed models. We also plan to bring our model closer to reality by considering the discrete nature of charges, non-electrostatic interactions, deviations from the idealized ge-

ometries of DNA and the histone core, including structural changes of the core, and chemical equilibrium between different states of the system.

Before we close this section, we will discuss the validity of our ground state analysis and critically evaluate how and under which circumstances thermal fluctuations of the DNA conformation can modify our results. Thermal effects come into play in three ways.

(i) First, for very dilute solutions of nucleosomal particles, the law of mass action dictates that uncomplexed histone proteins and DNA strands coexist with complexed structures. The balance between complexed and uncomplexed structures depends on the nucleosomal particle concentration, but also on the entropy content of the complex, which we made no effort to estimate in this paper. Our phase diagrams will not be modified by such effects for not too low concentrations.

(ii) Thermally activated fluctuations will smear out the boundaries between the various phases present in our phase diagrams. In order to examine the stability of the complexed state, we calculated the free energy difference between the ground states and a reference state (which is a straight DNA piece attached tangentially to the sphere). In Figs. 9(a) and 9(b) we show the parameter combinations for which this free energy difference equals  $5k_B T$  and  $10k_B T$  (dashed lines). It is obvious that for most parameter combinations thermal energy is much smaller than this free energy difference and we therefore conclude that the wrapped states we find via ground state analysis are thermodynamically stable. Clearly, all transition lines (which do not correspond to phase transitions in the thermodynamic sense) will be smeared out over a certain width, but based on our estimates the phases should still be detectable.

(iii) DNA fluctuations are suppressed in the tightly wrapped states and increase the free energy of those phases with respect to the unwrapped states. This effect can be expressed by undulation forces, which reflect the pronounced repulsion between polymers and confining surfaces [113]. The free energy of confinement of a piece of DNA (length  $L$  and persistence length  $l_0$ ) in a tube of diameter  $D$  is approximately  $F_{\text{conf}} \approx LD^{-2/3} l_0^{-1/3}$  [113]. Assuming the effective tube to have a diameter  $D \approx 2$  nm (this is a wild guess and based on nothing but the feeling that lateral fluctuations cannot be suppressed at length scales smaller than the diameter of the DNA itself and thereby yields an upper bound for the undulation free energy) we arrive for a single DNA turn around the histone with  $L \approx 30$  nm and  $l_0 = 30$  nm at  $F_{\text{conf}} \approx 5$  in units of  $k_B T$ . The bending energy of such a wrapped piece is of the order of  $F_{\text{bend}} \approx 20$  and thus much larger. Thus, undulation forces, though present, do not change our results considerably.

In summary, we conclude that the presence of thermal fluctuations do not invalidate the ground state results reported here.

#### APPENDIX A: ELECTROSTATIC ENERGY OF CHARGED RING

In this appendix we calculate in closed form the electrostatic energy associated with deforming a finite length

charged rod into a closed ring on the linearized Debye-Hückel level. This calculation sheds some light on the scale dependence of the electrostatic contribution to the persistence length [98] and discusses quite clearly the concept of the electrostatic closure energy. Most importantly, the resulting expression can be compared with our numerical results and allows to estimate the importance of discretization effects.

Suppose a charged line of length  $L$  and line charge density  $\tau$  is located in an ionic medium with screening length  $\kappa^{-1}$  and Bjerrum length  $l_B$ . We are interested in the energy difference between the ring configuration, where the line forms a closed circle, and the rod configuration, where the charged line is totally straight. Direct calculation of these two respective energies is difficult, even on the DH level. We therefore subtract from each configuration the energy of the pure Coulomb case, i.e., where the screening length is infinity, which renders all terms finite and computable (clearly, in the final expression, the pure Coulomb energies have to be added again).

The straight rod energy with the Coulomb energy subtracted reads

$$\begin{aligned} \frac{F_{\text{rod}}}{\tau^2 l_B / 2} &= \int_0^L ds \int_0^L ds' \frac{\exp(\kappa|s-s'|) - 1}{|s-s'|} \\ &= -\kappa \int_0^L ds \int_0^L ds' \left[ \int_0^1 d\beta \exp(-\beta\kappa|s-s'|) \right] \\ &= -\frac{2}{\kappa} [\exp(-\kappa L) - \kappa L \Gamma(0, \kappa L) + 1] \\ &\quad + 2L[1 - \ln(\kappa L) - \gamma]. \end{aligned} \quad (\text{A1})$$

In this expression,  $\gamma = 0.5772 \dots$  is Euler's constant and  $\Gamma(a, x)$  is the incomplete gamma function. Note that by construction this energy expression stays finite in the limit of vanishing salt concentration, i.e.,  $\kappa \rightarrow 0$ .

For the ring configuration we obtain (again subtracting the case of pure Coulomb interactions)

$$\begin{aligned} \frac{F_{\text{ring}}}{\tau^2 l_B / 2} &= L \int_0^L ds' \frac{\exp\left(-\frac{\kappa L}{\pi} \left| \sin \frac{\pi s'}{L} \right| \right) - 1}{\frac{L}{\pi} \left| \sin \frac{\pi s'}{L} \right|} \\ &= -L \int_0^\pi d\theta \int_0^{\kappa L / \pi} d\beta \exp(-\beta \sin \theta) \\ &= -\pi L \int_0^{\kappa L / \pi} d\beta [I_0(\beta) - L_0(\beta)] \\ &= -\kappa L^2 {}_1F_2 \left( \frac{1}{2}, \left( \frac{1}{3/2}, \frac{\kappa^2 L^2}{4\pi^2} \right) \right) \\ &\quad + \frac{\kappa^2 L^3}{\pi^2} {}_2F_3 \left( \left( \frac{1}{1}, \frac{3/2}{2} \right), \left( \frac{3/2}{2}, \frac{\kappa^2 L^2}{4\pi^2} \right) \right). \end{aligned} \quad (\text{A2})$$

In the intermediate expression,  $I_0$  denotes the modified Bessel function of zero order,  $L_0$  is Struve's function of zero order, and  ${}_pF_q$  are generalized hypergeometric functions [112].

The total energy difference between the ring and the rod configuration is given by

$$\Delta F = F_{\text{ring}} - F_{\text{rod}} + F_{\text{ring}}^{\text{Coul}} - F_{\text{rod}}^{\text{Coul}}, \quad (\text{A3})$$

where  $F_{\text{ring}}^{\text{Coul}}$  and  $F_{\text{rod}}^{\text{Coul}}$  are the pure Coulomb energies ( $\kappa = 0$ ) of the ring and rod configurations, respectively.

To calculate the difference between these Coulomb terms we need to regularize the interaction potentials by introducing a short-length cutoff  $\varepsilon$ . The rod Coulomb energy then reads

$$\frac{F_{\text{rod}}^{\text{Coul}}}{\tau^2 l_B / 2} = 2 \int_0^L ds \int_{s+\varepsilon}^L ds' \frac{1}{s'-s} = 2L(\ln L - 1 - \ln \varepsilon). \quad (\text{A4})$$

This expression diverges logarithmically for  $\varepsilon \rightarrow 0$ . The similarly regularized expression for the ring configuration reads

$$\begin{aligned} \frac{F_{\text{ring}}^{\text{Coul}}}{\tau^2 l_B / 2} &= L \int_{\varepsilon}^{L-\varepsilon} ds \frac{1}{\frac{L}{\pi} \left| \sin \frac{\pi s}{L} \right|} \\ &= L \left[ \ln \tan \frac{s}{2} \right]_{\varepsilon/\pi/L}^{\pi-\varepsilon/\pi/L} \\ &= 2L \left[ \ln \frac{\varepsilon \pi}{2L} + \frac{1}{3} \left( \frac{\varepsilon \pi}{2L} \right)^2 + O(\varepsilon^4) \right] \end{aligned} \quad (\text{A5})$$

and also diverges as the cutoff goes to zero. However, the difference between the two expressions Eqs. (A4) and (A5) stays finite in the limit  $\varepsilon \rightarrow 0$  and reads

$$\frac{F_{\text{ring}}^{\text{Coul}} - F_{\text{rod}}^{\text{Coul}}}{\tau^2 l_B / 2} = 2L \left( 1 - \ln \frac{\pi}{2} \right). \quad (\text{A6})$$

Putting all terms in Eqs. (A6) and (A2) together according to Eq. (A3), we find

$$\begin{aligned} \frac{\Delta F}{L \tau^2 l_B} &= \ln \kappa L - \ln(\pi/2) + \gamma - \frac{\kappa L}{2} {}_1F_2 \left( \frac{1}{2}, \left( \frac{1}{3/2}, \frac{\kappa L}{2\pi} \right)^2 \right) \\ &\quad + \frac{1}{2} \left( \frac{\kappa L}{\pi} \right)^2 {}_2F_3 \left( \left( \frac{1}{1}, \frac{3/2}{2} \right), \left( \frac{\kappa L}{2\pi} \right)^2 \right) \\ &\quad + \frac{1}{\kappa L} [1 - \exp(-\kappa L) + \kappa L \Gamma(0, \kappa L)]. \end{aligned} \quad (\text{A7})$$

The expressions (A7) can be expanded in the low-salt case, for  $\kappa L \ll 1$ , as

$$\frac{\Delta F}{L \tau^2 l_B} = 1 - \ln \frac{\pi}{2} + \left( \frac{2}{\pi^2} - \frac{1}{3} \right) (\kappa L)^2 + O([\kappa L]^4). \quad (\text{A8})$$

In the high-salt case, for  $\kappa L \gg 1$ , the following expansion holds [112]:

$$\frac{2}{\pi} \int_0^z d\beta [I_0(\beta) - L_0(\beta)] = \ln(2z) + \gamma - \sum_{k=1}^{\infty} \frac{(2k)!(2k-1)!}{(k!)^2 (2z)^{2k}}, \quad (\text{A9})$$

which allows the expansion of expressions (A2) and (A7) for  $\kappa L \gg 1$  with the result

$$\frac{\Delta F}{L \tau^2 l_B} = \frac{1}{\kappa L} + \frac{1}{2} \left( \frac{\pi}{\kappa L} \right)^2 + \frac{9}{4} \left( \frac{\pi}{\kappa L} \right)^4 + O([\kappa L]^{-6}). \quad (\text{A10})$$

All our results for the total electrostatic energy difference include in addition to the electrostatic bending energy also the electrostatic closure energy, which is the energy that is needed to connect the two ends of the line to a closed circle. In the following we will isolate this closure energy. As a side remark, we note that by symmetry, only terms of even order in the curvature of the PE (which is proportional to  $1/L$ ) should occur in the bending energy. The first term in Eq. (A10) is of odd order, but this term will now be shown to be related to the closure energy and can thus be eliminated by suitable subtraction. To explicitly obtain this closure energy, we calculate the electrostatic energy needed to connect  $n$  rods of length  $L/n$  to one rod of length  $L$ , which reads

$$\begin{aligned} \frac{F_{\text{close}}}{l_B \tau^2} &= \int_0^L ds \int_s^L ds' \frac{e^{-\kappa(s'-s)}}{s'-s} - n \int_0^{L/n} ds \int_s^{L/n} ds' \frac{e^{-\kappa(s'-s)}}{s'-s} \\ &= \sum_{i=0}^{n-1} \int_{iL/n}^{(i+1)L/n} ds \int_{-s+(i+1)L/n}^{L-s} ds' \frac{e^{-\kappa s'}}{s'} \\ &= \kappa^{-1} \left[ n \int_0^{\kappa L/n} dz \Gamma(0, z) - \int_0^{\kappa L} dz \Gamma(0, z) \right]. \end{aligned} \quad (\text{A11})$$

Sending the length of the rod segments to infinity,  $\kappa L/n \rightarrow \infty$ , we neglect the finite length of the subrods and end up with

$$F_{\text{close}} = \frac{\tau^2 l_B}{\kappa} (n-1), \quad (\text{A12})$$

which is the closure energy to connect  $n$  rods to a single rod (in the limit when the rods are much longer than the screening length). Clearly, the closure energy of a single connection is obtained by choosing  $n=2$ , in which case we obtain

$$F_{\text{close}} = \frac{\tau^2 l_B}{\kappa}. \quad (\text{A13})$$

This is the first term in Eq. (A10). Subtracting this constant, we obtain the electrostatic bending energy without any additional contributions from the closure energy and which thus

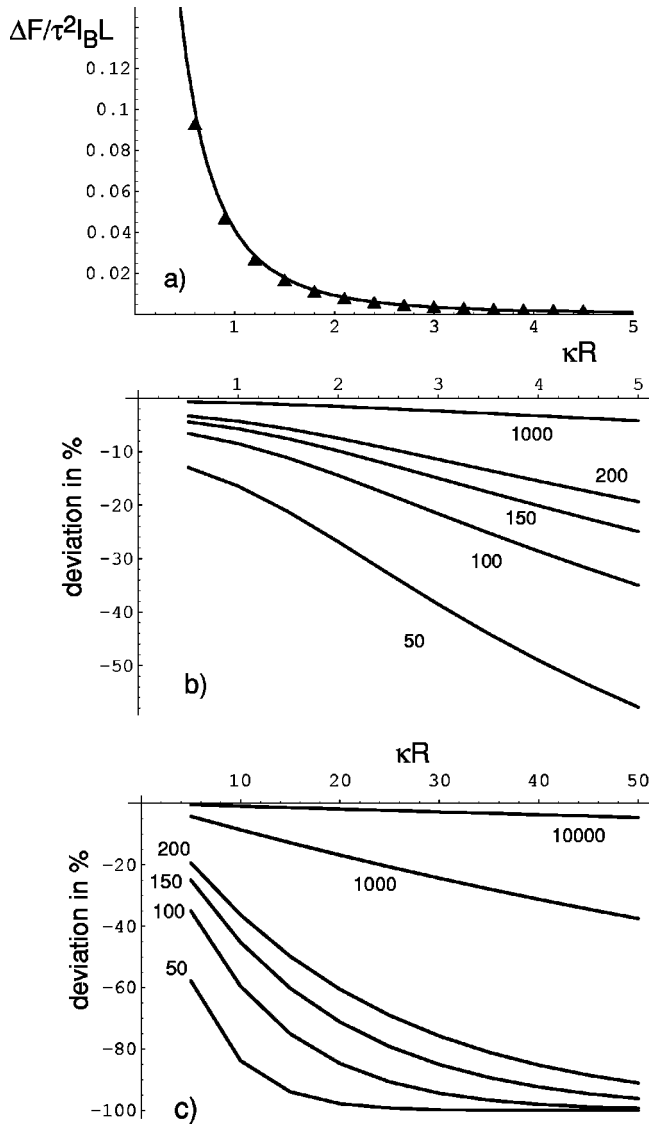


FIG. 26. (a) Electrostatic contribution to the bending energy for a closed ring as a function of the rescaled inverse screening length. The solid line denotes the analytical result Eq. (A7) and the data points are based on a numerical discrete sum with 100 discretization points. (b), (c) Deviation of the numerical summation from the analytical calculation in percent for different numbers of discretization points.

can be compared with previous results. Consider the bending energy of a Kratky-Porod chain with persistence length  $l_{OSF}$  bent into a circle with radius  $R=L/2\pi$ . The bending energy of the chain is  $F_{bend}=\pi l_{OSF}/R$ . If we compare the quadratic term of Eq. (A10) with this expression, we obtain  $l_{OSF}=\tau^2 l_B/(4\kappa^2)$ , which is the standard expression for the electrostatic contribution to the persistence length [93,94]. This approximation breaks down for  $\kappa R < 2\pi$  as an inspection of Eq. (A10) shows. In the case of DNA wrapping around a histone, the bending radius is about 5 nm. This implies that one needs  $\kappa \gg 1 \text{ nm}^{-1}$  in order for the Odijk-Skolnick-Fixman expression  $l_{OSF}$  to be accurate. However, for fully dissociated DNA and  $\kappa=1 \text{ nm}^{-1}$ , the electrostatic persistence length is  $l_{OSF} \approx 6 \text{ nm}$  and for  $\kappa=2 \text{ nm}^{-1}$  it is only

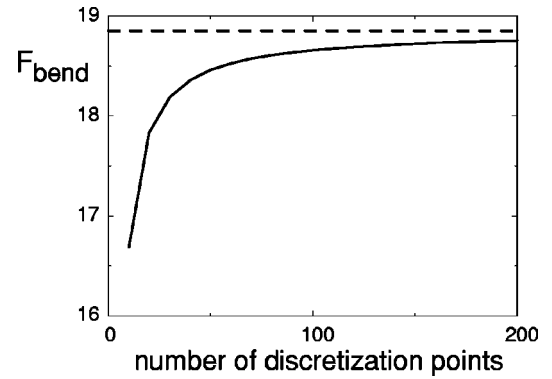


FIG. 27. Mechanical bending energy for a ring of radius 5 nm and bare persistence length  $l_0=30 \text{ nm}$ . The broken line denotes the result in the continuum limit,  $F_{bend}=\pi l_0/R$ , while the solid line results from the numerical integration for varying number of discretization points.

$l_{OSF} \approx 1.5 \text{ nm}$ . The mechanical persistence length of DNA is  $l_0=30 \text{ nm}$ . We therefore conclude that in our problem either the Odijk-Skolnick-Fixman persistence length  $l_{OSF}$  is not valid (for  $\kappa < 1 \text{ nm}^{-1}$ ), or it is negligible compared to the mechanical persistence length (for  $\kappa > 1 \text{ nm}^{-1}$ ). This stresses that it is important to explicitly evaluate the electrostatic bending energy in the DNA-histone binding problem, as we have done throughout this paper.

## APPENDIX B: DISCRETIZATION EFFECTS

Discretization effects have been discussed at length in Sec. IV D in connection with artifacts related to the breaking of the rotational symmetry. A more fundamental discretization effect is due to the fact that in the energy contributions entering the free energy equation (1), we approximate integrals by sums, so that the final outcome depends on the number of discretization steps that are used to represent the DNA conformation. In order to estimate the error caused by this numerical integration we first numerically calculate the electrostatic (DH) and mechanical bending energy of a closed ring and compare it with analytical expressions valid in the continuum limit.

We first consider the electrostatic bending energy of a charged polymer of length  $2\pi R$ , which is bent into a circle with radius  $R$ , which has been calculated analytically in Appendix A. In Fig. 26(a) we show the comparison of numerical calculations for 100 discretization points with the analytical solution given in Eq. (A7) as a function of the inverse screening length. Overall, the agreement is quite good. Closer inspection of the relative error, done in Figs. 26(b) and 26(c) for different numbers of discretization steps, reveals substantial deviations for large salt concentrations and for small numbers of discretization steps. As an example, for  $\kappa R \approx 5$ , which for a histone protein of effective radius  $R \approx 5 \text{ nm}$  corresponds to a physiological salt concentration, and a discretization with 100 points for a piece of length  $2\pi R$  (which corresponds to about 200 points for a total length  $L=50 \text{ nm}$ , as was used in the main part of our paper), we underestimate the electrostatic bending energy by

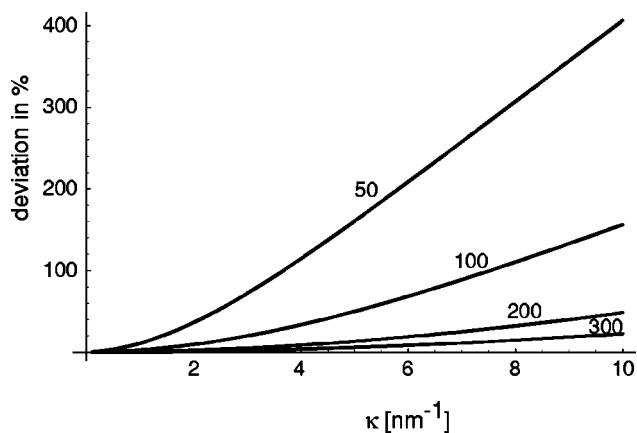


FIG. 28. Electrostatic energy between a charged sphere and a straight DNA segment which extends radially away from the sphere. Shown is the deviation of numerical results from the analytical prediction in percent and as a function of the number of discretization steps.

$\approx 30\%$ , which constitutes a large error. However, as we will show in the following, the situation is not so bad, as for large salt concentration, the total bending energy starts to be dominated by the mechanical contribution, and the large errors in the electrostatic contribution do not matter much for the determination of phase boundaries, as we will explicitly demonstrate. Still, it is interesting and important to note that discretization effects become quite pronounced at moderately large salt concentrations, but become unimportant at low salt concentrations and, in particular, at zero salt in the Coulomb limit. This result is of course connected to the fact that the Coulomb interaction is very long ranged such that small length scale effects become irrelevant at large length scales.

In Fig. 27 we show the mechanical bending energy for a ring of radius  $R=5$  nm and persistence length  $l_0=30$  nm as a function of different numbers of discretization points (solid line). The broken line denotes the continuum result, which is  $F_{bend} = \pi l_0 / R$ . Above 100 discretization points the accuracy is within 1%. Above  $\kappa R \approx 5$  the total bending energy is dominated by the mechanical persistence length, such that the strong deviations in the electrostatic contribution for  $\kappa R > 5$  do not influence the results, as we will demonstrate shortly.

We next address discretization effects on the interaction between the sphere and the DNA. In Fig. 28 we show the deviation of the numerically determined electrostatic energy

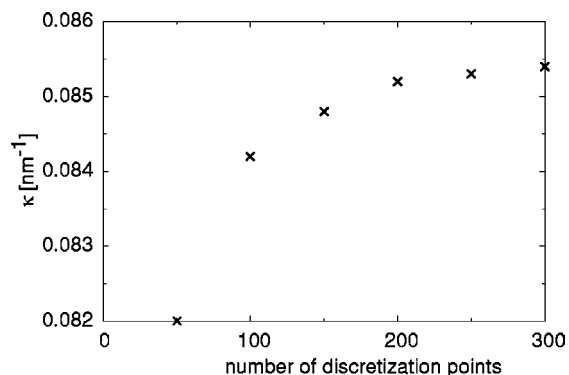


FIG. 29. Locus of rotational symmetry transition point vs discretization for  $Z=40$ .

for a straight DNA segment of length  $L=49.6$  nm, starting at distance  $R=5$  nm from the origin and extending radially, from the exact continuum result. The DNA interacts with a charge in the origin via the DH potential as defined in Eq. (1). The deviation of numerical integration from analytic calculation depends on the salt concentration and on the number of discretization points. As for the DNA self-interaction, the error becomes larger as the salt concentration increases, but for the range of salt concentrations where we obtain most of our results, the error is not larger than a few percent. In contrast, for a polymer wrapped around the sphere, the numerical integration reproduces the continuum result exactly due to the symmetry of the problem. Since the collapsed state and the straight line are extreme conformations of the polymer, the error of our calculations is usually smaller than given in Fig. 28.

As a check of the interplay of all different discretization effects discussed here, we show in Fig. 29 the variation of the location of the transition that breaks the rotational symmetry at a sphere charge of  $Z=40$  as a function of the number of discretization points. We see that above 200 discretization points the transition value changes only very slightly.

In summary, the deviations due to discretization effects in the electrostatic parts of the free energy, Eq. (1), increase strongly with increasing salt concentration. Discretization errors in the mechanical bending energy are, in general, unimportant. In the regime of salt concentrations where most of the phase transitions occur, 200 discretization points approximate the continuum model sufficiently well, meaning that the phase boundaries reported in this paper reflect the continuum limit with sufficient accuracy.

[1] P.L. Dubin, M.E. Curran, and J. Hua, *Langmuir* **6**, 707 (1990).  
 [2] D.W. McQuigg, J.I. Kaplan, and P.L. Dubin, *J. Phys. Chem.* **96**, 1973 (1992).  
 [3] P. Haronska, T.A. Vilgis, R. Grottenmüller, and M. Schmidt, *Macromol. Theory Simul.* **7**, 241 (1998).  
 [4] H. Zhang *et al.*, *J. Phys. Chem. B* **103**, 2347 (1999).  
 [5] G.B. Sukhorukov *et al.*, *Polym. Adv. Technol.* **9**, 759 (1998).

[6] F. Caruso, R. Caruso, and H. Möhwald, *Science* **282**, 1111 (1998).  
 [7] D.I. Gittins and F. Caruso, *Adv. Mater.* **12**, 1947 (2000).  
 [8] D.I. Gittins and F. Caruso, *J. Phys. Chem. B* **105**, 6846 (2001).  
 [9] J.D. McGhee and G. Felsenfeld, *Annu. Rev. Biochem.* **49**, 1115 (1980).  
 [10] R.D. Kornberg and A. Klug, *Sci. Am.* **244**(2), 48 (1981).

- [11] J. Widom, *Annu. Rev. Biophys. Biophys. Chem.* **18**, 365 (1989).
- [12] G. Felsenfeld, *Nature (London)* **355**, 219 (1992).
- [13] K. van Holde, *Nature (London)* **362**, 111 (1993).
- [14] G. Felsenfeld, *Cell* **86**, 13 (1996).
- [15] K. Luger and T.J. Richmond, *Curr. Opin. Struct. Biol.* **8**, 33 (1998).
- [16] F. Ganachaud *et al.*, *Langmuir* **13**, 701 (1997).
- [17] A.U. Bielinska, J.F. Kukowska-Latallo, and J.R. Baker Jr., *Biochim. Biophys. Acta* **1353**, 180 (1997).
- [18] F. von Goeler and M. Muthukumar, *J. Chem. Phys.* **100**, 7796 (1994).
- [19] E. Gurovitch and P. Sens, *Phys. Rev. Lett.* **82**, 339 (1999).
- [20] R. Golestanian, *Phys. Rev. Lett.* **83**, 2473 (1999).
- [21] N.L. Marky and G.S. Manning, *Biopolymers* **31**, 1543 (1991).
- [22] N.L. Marky and G.S. Manning, *J. Mol. Biol.* **254**, 50 (1995).
- [23] R.R. Netz and J.-F. Joanny, *Macromolecules* **32**, 9026 (1999).
- [24] H. Schiessel, J. Rudnick, R.F. Bruinsma, and W.M. Gelbart, *Europhys. Lett.* **51**, 237 (2000).
- [25] E.M. Mateescu, C. Jeppesen, and F. Pincus, *Europhys. Lett.* **46**, 493 (1999).
- [26] T.T. Nguyen and B.I. Shklovskii, *Physica A* **293**, 324 (2001).
- [27] T.T. Nguyen and B.I. Shklovskii, *J. Chem. Phys.* **114**, 5905 (2001).
- [28] H. Schiessel, R.F. Bruinsma, and W.M. Gelbart, *J. Chem. Phys.* **115**, 7245 (2001).
- [29] S.Y. Park, R.F. Bruinsma, and W.M. Gelbart, *Europhys. Lett.* **46**, 454 (1999).
- [30] K.K. Kunze and R.R. Netz, *Europhys. Lett.* **58**, 299 (2002).
- [31] R.R. Netz and J.-F. Joanny, *Macromolecules* **32**, 9013 (1999).
- [32] T. Wallin and P. Linse, *Langmuir* **12**, 305 (1996).
- [33] T. Wallin and P. Linse, *J. Phys. Chem.* **100**, 17873 (1996).
- [34] T. Wallin and P. Linse, *J. Phys. Chem.* **101**, 5506 (1997).
- [35] P. Chodanowski and S. Stoll, *Macromolecules* **34**, 2320 (2001).
- [36] M. Jonsson and P. Linse, *J. Chem. Phys.* **115**, 3406 (2001); **115**, 10 975 (2001).
- [37] C.L. Woodcock, S.A. Grigoryev, R.A. Horowitz, and N. Whitaker, *Proc. Natl. Acad. Sci. U.S.A.* **90**, 9021 (1993).
- [38] J. Bednar, R.A. Horowitz, S.A. Grigoryev, L.M. Carruthers, J.C. Hansen, A.J. Koster, and C.L. Woodcock, *Proc. Natl. Acad. Sci. U.S.A.* **95**, 14173 (1998).
- [39] J.A. Martino, V. Katritch, and W.K. Olson, *Structure (London)* **7**, 1009 (1999).
- [40] H. Schiessel, W.M. Gelbart, and R.F. Bruinsma, *Biophys. J.* **80**, 1940 (2001).
- [41] E. Ben-Haim, A. Lesne, and J.-M. Victor, *Phys. Rev. E* **64**, 051921 (2001).
- [42] D.J. Clark and T. Kimura, *J. Mol. Biol.* **211**, 883 (1990).
- [43] D.A. Beard and T. Schlick, *Structure (London)* **9**, 105 (2001).
- [44] K.K. Kunze and R.R. Netz, *Phys. Rev. Lett.* **85**, 4389 (2000).
- [45] L. Stryer, *Biochemistry* (Freeman, New York, 1995).
- [46] T.J. Richmond, J.T. Finch, B. Rushton, D. Rhodes, and A. Klug, *Nature (London)* **311**, 532 (1984).
- [47] K. Luger, A.W. Mäder, R.K. Richmond, D.F. Sargent and T.J. Richmond, *Nature (London)* **389**, 251 (1997).
- [48] J. Bednar, R.A. Horowitz, J. Dubochet and C.L. Woodcock, *J. Cell Biol.* **131**, 1365 (1995).
- [49] C.L. Woodcock and R.A. Horowitz, *Methods Enzymol.* **12**, 84 (1997).
- [50] J. Zlatanova, S.H. Leuba, G. Yang, C. Bustamente, and K. van Holde, *Proc. Natl. Acad. Sci. U.S.A.* **91**, 5277 (1994).
- [51] S.H. Leuba, G. Yang, C. Robert, B. Samori, K. van Holde, J. Zlatanova, and C. Bustamente, *Proc. Natl. Acad. Sci. U.S.A.* **91**, 11621 (1994).
- [52] C. Bustamente, G. Zuccheri, S.H. Leuba, G. Yang, and B. Samori, *Methods Enzymol.* **12**, 73 (1997).
- [53] G. Arents and E.N. Moudrianakis, *Proc. Natl. Acad. Sci. U.S.A.* **92**, 11170 (1995).
- [54] G. Arents and E.N. Moudrianakis, *Proc. Natl. Acad. Sci. U.S.A.* **90**, 10489 (1993).
- [55] K.J. Polach and J. Widom, *J. Mol. Biol.* **254**, 130 (1995).
- [56] P. Bhargava, *Protein Sci.* **2**, 2233 (1993); **2**, 2246 (1993).
- [57] D. Rhodes and A. Klug, *Nature (London)* **286**, 573 (1980).
- [58] J.J. Hayes, T.D. Tullius, and A.P. Wolffe, *Proc. Natl. Acad. Sci. U.S.A.* **87**, 7405 (1990).
- [59] Y. Cui and C. Bustamente, *Proc. Natl. Acad. Sci. U.S.A.* **97**, 127 (2000).
- [60] M.L. Bennink *et al.*, *Nat. Struct. Biol.* **8**, 606 (2001).
- [61] J.F. Marko and E.D. Siggia, *Biophys. J.* **73**, 2173 (1997).
- [62] J.D. McGhee and G. Felsenfeld, *Nucleic Acids Res.* **8**, 2751 (1980).
- [63] W.O. Weischet, K. Tatchell, K.E. van Holde, and H. Klump, *Nucleic Acids Res.* **5**, 139 (1978).
- [64] V.C. Gordon, V.N. Schumaker, D.E. Olins, C.M. Knobler, and J. Horwitz, *Nucleic Acids Res.* **6**, 3845 (1979).
- [65] R.T. Simpson, *J. Biol. Chem.* **254**, 10 123 (1979).
- [66] V.C. Gordon, C.M. Knobler, D.E. Olins, and V.N. Schumaker, *Proc. Natl. Acad. Sci. U.S.A.* **75**, 660 (1978).
- [67] G. Russev, L. Vassilev, and R. Tsanev, *Mol. Biol. Rep.* **6**, 45 (1980).
- [68] J.B.E. Burch and H.G. Martinson, *Nucleic Acids Res.* **8**, 4969 (1980).
- [69] J. Ausio, D. Seger, and H. Eisenberg, *J. Mol. Biol.* **176**, 77 (1984).
- [70] R.E. Harrington, *Biopolymers* **20**, 719 (1981).
- [71] R.E. Harrington, *Biochemistry* **21**, 1177 (1982).
- [72] E.C. Uberbacher, V. Ramakrishnan, D.E. Olins, and G.J. Bunick, *Biochemistry* **22**, 4916 (1983).
- [73] A.E. Dieterich, R. Axel, and C.R. Cantor, *J. Mol. Biol.* **129**, 587 (1979).
- [74] L.J. Libertini and E.W. Small, *Nucleic Acids Res.* **8**, 3517 (1980).
- [75] L.J. Libertini and E.W. Small, *Biochemistry* **21**, 3327 (1982).
- [76] L.J. Libertini and E.W. Small, *Nucleic Acids Res.* **15**, 6655 (1987).
- [77] I. Oohara and A. Wada, *J. Mol. Biol.* **196**, 399 (1987).
- [78] D.W. Brown, L.J. Libertini, and E.W. Small, *Biochemistry* **30**, 5293 (1991).
- [79] S.N. Khrapunov, A.I. Dragan, A.V. Sivolob, and A.M. Zagaraya, *Biochim. Biophys. Acta* **1351**, 213 (1997).
- [80] T.D. Yager and K.E. van Holde, *J. Biol. Chem.* **259**, 4212 (1984).
- [81] S. Mangenot, A. Leforestier, P. Vachette, D. Durant, and F. Livolant, *Biophys. J.* **82**, 345 (2002).
- [82] F. Dong, C. Nelson, and J. Ausio, *Biochemistry* **29**, 10 710 (1990).

- [83] S. Mangenot, E. Raspaud, C. Tribet, L. Belloni, and F. Livolant (unpublished).
- [84] T.D. Yager, C.T. McMurray, and K.E. van Holde, *Biochemistry* **28**, 2271 (1989).
- [85] B.D. Strahl and D. Allis, *Nature (London)* **403**, 41 (2000).
- [86] S.R. Roth and C.D. Allis, *Cell* **87**, 5 (1996).
- [87] J.P. Whitlock and A. Stein, *J. Biol. Chem.* **253**, 3857 (1978).
- [88] T. Sakaue, K. Yoshikawa, S.H. Yoshimura, and K. Takeyasu, *Phys. Rev. Lett.* **87**, 078105 (2001).
- [89] J.K. Strauss and L.J. Maher, *Science* **266**, 1829 (1994).
- [90] G.S. Manning, K.K. Ebralidse, A.D. Mirzabekov, and A. Rich, *J. Biomol. Struct. Dyn.* **6**, 877 (1989).
- [91] A.Y. Grosberg and A.R. Khokhlov, *Statistical Physics of Macromolecules* (AIP, Woodbury, NY, 1994).
- [92] P.J. Hagerman, *Annu. Rev. Biophys. Biophys. Chem.* **17**, 265 (1988).
- [93] T. Odijk, *J. Polym. Sci. A* **15**, 477 (1977).
- [94] J. Skolnick and M. Fixman, *Macromolecules* **10**, 944 (1977).
- [95] N. Borochof, H. Eisenber, and Z. Kam, *Biopolymers* **20**, 231 (1981).
- [96] G.S. Manning, *Biopolymers* **20**, 1751 (1981).
- [97] E.S. Sobel and J.A. Harpst, *Biopolymers* **31**, 1559 (1991).
- [98] J.-L. Barrat and J.-F. Joanny, *Europhys. Lett.* **24**, 333 (1993).
- [99] G.S. Manning, *Q. Rev. Biophys.* **2**, 179 (1978).
- [100] M. le Bret, *J. Chem. Phys.* **76**, 6243 (1982).
- [101] M. Fixman, *J. Chem. Phys.* **76**, 6346 (1982).
- [102] Even for the relatively simple problem of the adsorption of a single DNA modeled by a rigid charged cylinder on an oppositely charged plane, the accurate numerical solution of the PB equation is nontrivial, see C. Fleck, R.R. Netz, and H.H. von Grünberg, *Biophys. J.* **82**, 76 (2002).
- [103] R.R. Netz, *Phys. Rev. E* **60**, 3174 (1999).
- [104] P.T. Lowary and J. Widom, *J. Mol. Biol.* **276**, 19 (1998).
- [105] P.T. Lowary and J. Widom, *Proc. Natl. Acad. Sci. U.S.A.* **94**, 1183 (1997).
- [106] E.J.W. Verwey and J.T.G. Overbeek, *Theory of the Stability of Lyophobic Colloids* (Elsevier, New York, 1948).
- [107] R.R. Netz and J.-F. Joanny, *Macromolecules* **31**, 5123 (1998).
- [108] NAG FORTRAN Library, ©Numerical Algorithms Group, 256 Banbury Road, Oxford, OX27DE, U.K.
- [109] P.E. Gill, W. Murray, M.A. Saunders, and M.H. Wright. User's guide for NPSOL (Version 4. 0). *Report SOL 86-2* (Department of Operations Research, Stanford University, 1986).
- [110] A. Gray, *Modern Differential Geometry of Curves and Surfaces* (Spektrum Akademischer Verlag, Heidelberg, 1994) (in German).
- [111] F. Oosawa, *Polyelectrolytes* (Marcel Dekker, New York, 1971).
- [112] *Handbook of Mathematical Functions*, edited by M. Abramowitz and I. A. Stegun, 9th ed. (Dover, New York, 1972).
- [113] T. Odijk, *Macromolecules* **16**, 1340 (1983); **17**, 502 (1984).